ACCEPTED VERSION

Siew Yee Lim, Cheryl Suwen Law, Lina Liu, Marijana Markovic, Andrew D. Abell and Abel Santos

Integrating surface plasmon resonance and slow photon effects in nanoporous anodic alumina photonic crystals for photocatalysis

Catalysis Science and Technology, 2019; 9(12):3158-3176

Published at: http://dx.doi.org/10.1039/c9cy00627c

ROYAL SOCIETY OF CHEMISTRY View Article Online
DOI: 10.1039/C9CY00627C

Catalysis Science & Technology

ARTICLE

Integrating Surface Plasmon Resonance and Slow Photon Effects in Nanoporous Anodic Alumina Photonic Crystals for Photocatalysis

Received 00th January 2019,
Accepted 00th January 2019

DOI: 10.1039/x0xx00000x

www.rsc.org/

Siew Yee Lim[a,b,c], Cheryl Suwen Law[a,b,c], Lina Liu[a,d], Marijana Markovic[a,e], Andrew D. Abell[*b,c,f] and Abel Santos[*a,b,c]

This study explores the potential of gold-coated titania-functionalized nanoporous anodic alumina distributed Bragg reflectors (Au-TiO_2-NAA-DBRs) as platforms to enhance photocatalytic reactions by integrating "slow photons" and surface plasmon resonance (SPR). The photocatalytic degradation rate of methylene blue – a model organic compound with a well-defined absorbance band in the visible spectral region – by these composite photonic crystals (PC) upon visible–NIR light irradiation is used as an indicator to identify coupling effects between "slow photon" effect and SPR. Our study demonstrates that the photocatalytic enhancement in Au-TiO_2-NAA-DBRs is strongly associated with "slow photons" effect, while the contribution of SPR to the overall photocatalytic enhancement is weak due to the localized generation of surface plasmons on the top surface of the composite PC structure. Photocatalytic enhancement is optimal when the characteristic photonic stopband of these PCs partially overlaps with the absorbance band of methylene blue, which results in edges being positioned away from the absorbance maximum of the organic dye. The overall photocatalytic degradation for methylene blue is also correlated to the type of noble metal coating and the geometric features of the PC structures. These results establish a rationale for further development of noble metal-coated NAA-based hybrid plasmonic–photonic crystal photocatalyst platforms to optimally integrate "slow photons" and SPR for enhancing the efficiency of photocatalytic reactions and other light harvesting applications.

Introduction

Semiconductor photocatalysts harvest the energy of incoming photons to drive chemical reactions for solar-to-fuel conversion and environmental remediation, including hydrogen (H_2) energy generation,[1-3] water treatment,[4-11] air purification,[12,13] ammonia (NH_3) synthesis,[14,15] carbon dioxide (CO_2) reduction[16,17] and warfare agents destruction.[18,19] In land-mark studies, Fujishima[20] and Carey[21] reported production of clean H_2 energy and degradation of organic pollutants by semiconducting titanium dioxide (TiO_2) under UV light irradiation, respectively. TiO_2 remains a benchmark semiconducting material for photocatalysis applications due to its strong oxidizing capability, remarkable stability against photo- and chemical corrosion, non-toxicity and low cost.[22] However, the high recombination rate of electron/hole (e^-/h^+) pairs (i.e. ~90%) and the large energy bandgap (i.e. ~3.0–3.2 eV) of TiO_2 only enables efficient absorption of UV light (i.e. ~4% of the solar spectrum), limiting the practical capability of this material for sunlight-driven photocatalysis applications.[23]

Various approaches have been devised to overcome the intrinsic limitations of TiO_2, including doping,[24,25] coupling with other semiconducting metal oxides,[26,27] surface modification,[28,29] engineering of mesoporous structures[30,31] and incorporation of noble metals.[7-9,32] Enhanced photocatalytic performance of hybrid noble metal/TiO_2 composite structures is associated with localized surface plasmon resonances (SPR), which are collective oscillations of the conducting electrons in the noble metal driven by the electromagnetic field generated by incident photons.[33,34] For instance, Lu et al. (2012)[5] demonstrated that hybrid Au nanoparticle-decorated–TiO_2 nanocrystalline platforms have ~52% superior performance compared to uncoated TiO_2 nanocrystalline particles in the photocatalytic degradation of 2,4-dichlorophenol under visible light irradiation. This photocatalytic enhancement is associated with SPR, which can extend absorption of the semiconductor material to a wavelength longer range (i.e. visible spectrum), while also reducing the recombination rate of e^-/h^+ pairs by forming a heterojunction between the semiconductor and the noble metal. Photocatalytic reactions can be further enhanced by engineering the structure of hybrid noble metal–TiO_2

[a] School of Chemical Engineering, The University of Adelaide, 5005 Adelaide, Australia
[b] Institute for Photonics and Advanced Sensing (IPAS), The University of Adelaide, 5005 Adelaide, Australia
[c] ARC Centre of Excellence for Nanoscale BioPhotonics (CNBP), The University of Adelaide, 5005 Adelaide, Australia
[d] School of Chemistry and Chemical Engineering, Ningxia University, 7520021 Yinchuan, P.R. China
[e] Center of Chemistry, Institute of Chemistry, Technology and Metallurgy, University of Belgrade, 11000 Belgrade, Serbia
[f] Department of Chemistry, The University of Adelaide, 5005 Adelaide, Australia
* E-Mails: andrew.abell@adelaide.edu.au ; abel.santos@adelaide.edu.au

photocatalyst materials in the form of photonic crystals (PCs), including nanotubes,[35] inverse opals[5,36] and bioinspired PC structures.[37] For instance, hybrid Au nanoparticle-decorated–TiO_2 inverse opal PC structures outperform Au nanoparticle-decorated–TiO_2 nanocrystalline counterparts, with ~56% enhancement in the photodegradation of the same organic pollutant.[5] PC structures can enhance light–matter interactions for photocatalysis via Bragg diffraction, multiple scattering and "slow photon" effect.[9,38-40] Bragg diffraction inhibits propagation of light within the spectral range of the PC's photonic stopband (PSB). However, multiple scattering increases the confinement of light at those wavelengths away from the PSB so light trapped within the PC's structure can be used by the semiconductor to speed up photocatalytic reactions. "Slow photon" effect occurs at the frequency edges of the PSB, where slow photons (i.e. photons with strongly reduced group velocity) are primarily localized in the high (i.e. red edge of the PSB) and low (i.e. blue edge of the PSB) dielectric parts of the PC's structure. This effect significantly increases the lifetime of photons and the overall light absorption of the semiconductor. Coupling of SPR and PC effects in hybrid noble metal–TiO_2 PC photocatalyst structures can thus significantly enhance the overall photon-to-electron conversion rate by a rational management of photons at the nanoscale. However, the fabrication of TiO_2-based PCs presents intrinsic limitations and technical challenges, including limited spectral controllability of the PC's PSB features, restriction to small areas and long processing times (i.e. TiO_2-based inverted opal PCs), and light scattering due to the over-etching of the PC structure in hydrofluoric acid (HF)-based electrolytes (i.e. TiO_2-based nanotubular PCs produced by anodization). These drawbacks limit practical utilization of TiO_2-based PCs for efficient and large-scale photocatalytic applications.[41-46]

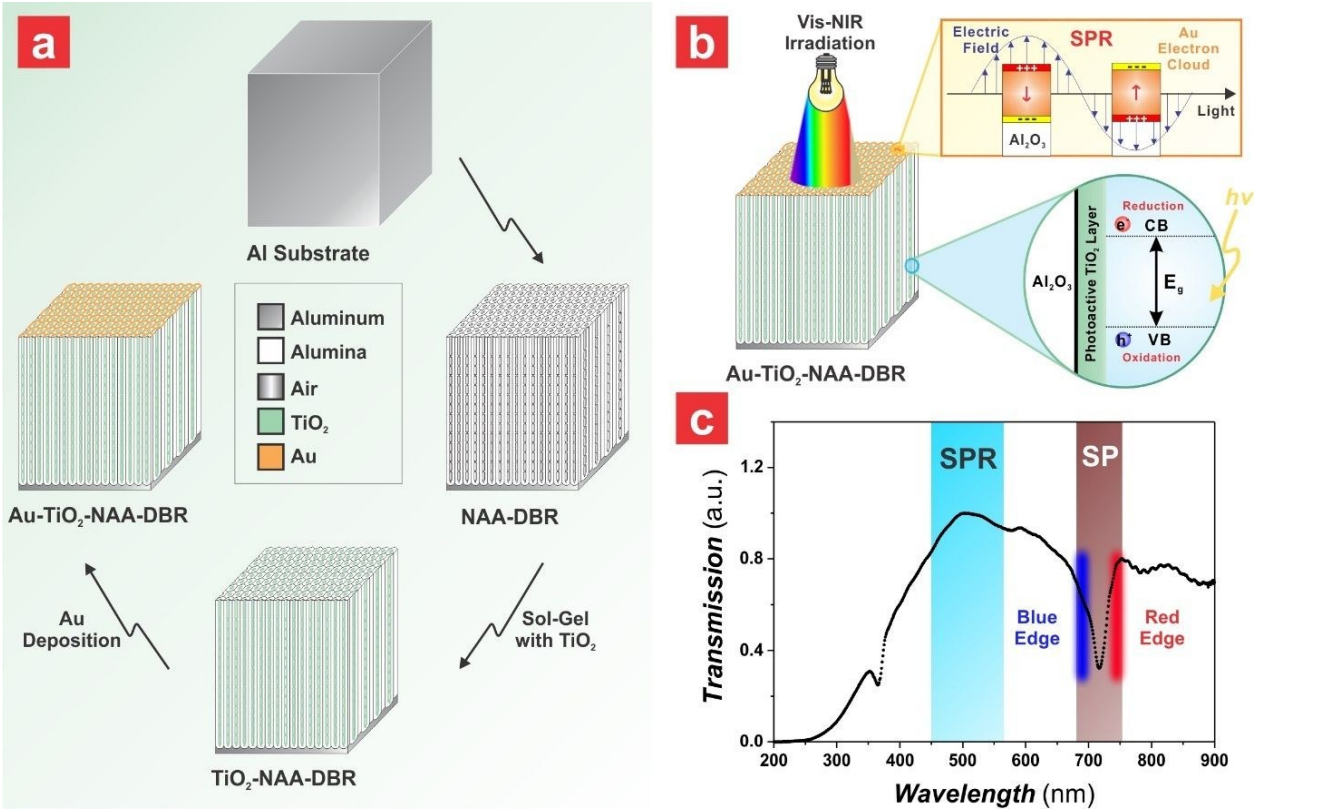

Fig. 1 Fabrication of gold-coated titania-functionalized nanoporous anodic alumina distributed Bragg reflectors (Au-TiO_2-NAA-DBRs) by two-step pulse anodization for their application in photocatalysis. a) Schematic showing the fabrication of Au-TiO_2-NAA-DBRs by two-step pulse anodization, surface functionalization with photoactive TiO_2 and deposition of metallic Au. b) Schematic illustrating the photocatalytic assessment of Au-TiO_2-NAA-DBRs under controlled visible–NIR irradiation conditions, with details showing the surface plasmon resonance (SPR) (top) and the chemical and electronic band structures (bottom) of the composite PC structures (note: E_g = energy bandgap, *hv* = excitation energy, CB = conduction band and VB = valence band). c) Transmission spectrum of a reference Au-TiO_2-NAA-DBR showing the region of "slow photon" (SP) effect induced by the blue and red edges of the photonic stopband (PSB) and the SPR effect associated with the metallic Au film on the top of the PC structure (note: Au-TiO_2-NAA-DBR produced with anodization period – T_P = 985 s, pore widening time – t_{pw} = 24 min, Au deposition time – τ_D = 30 s and medium = air).

Significant effort has been devoted to large scale production of alternative materials that can be engineered into high-performing TiO_2-based PC photocatalyst platforms for real-life applications. We have recently demonstrated that TiO_2-functionalized nanoporous anodic alumina photonic crystals (NAA-PCs), with rationally engineered optical properties, provide superior performance than that of conventional photocatalyst platforms in the photodegradation of a variety of organic pollutants.[10,11] NAA is an ideal platform to develop PC structures due to its highly controllable and versatile nanoporous structure composed of cylindrical nanopores. The optical features of the characteristic PSB in NAA-PCs can be modulated with precision by engineering their nanoporous structure in the form of different PC architectures,

including distributed Bragg reflectors (DBRs),[11,47] bandpass filters,[48,49] Fabry-Pérot interferometers,[50,51] gradient-index filters,[10,52-54] hybrid photonic crystals,[55] and optical microcavities.[56-58] NAA-PCs have been used in optical chemo- and biosensing,[50,51] light filtering,[47] optical encoding[54] and photocatalysis.[10,11] The nanoporous structure of NAA-PCs facilitates mass transfer of ionic and molecular species involved in photocatalytic reactions and an efficient management of photons by controlled light–matter interactions to increase photon-to-electron conversion rates for high-performance photocatalytic applications.[4,10,11]

In this study, we analyze the photocatalytic performance of hybrid Au-TiO_2-NAA-DBRs by monitoring the photodegradation of a model organic. Au-TiO_2-NAA-DBRs are fabricated by two-step pulse anodization and chemically modified by sol-gel method and deposition of Au (**Fig. 1**). The effect of various fabrication parameters (i.e. anodization period, pore widening time, noble metal deposition time, starting anodization voltage and type of noble metal coating) on the photocatalytic performance of these hybrid PCs under controlled visible–NIR irradiation are systematically investigated. The photocatalytic degradation of methylene blue by Au-TiO_2-NAA-DBRs allows the identification and quantification of photocatalytic performance enhancements associated with coupling effects between slow photons and SPR.

Experimental Section

Materials

High purity (99.9997%) aluminum (Al) foils 0.32 mm thick were supplied by Goodfellow Cambridge Ltd. (UK). Oxalic acid ($H_2C_2O_4$), perchloric acid ($HClO_4$), copper (II) chloride ($CuCl_2$), hydrochloric acid (HCl), chromic acid (H_2CrO_4), titanium (IV) butoxide ($Ti(OBu)_4$), hydrogen peroxide (H_2O_2) and methylene blue ($C16H18ClN3S$, MB) were purchased from Sigma-Aldrich (Australia). Ethanol (C_2H_5OH, EtOH) and phosphoric acid (H_3PO_4) were supplied by ChemSupply (Australia). Aqueous solutions used in this study were prepared with ultrapure Milli-Q® water (18.2 mΩ·cm).

Fabrication of NAA-DBRs

NAA-DBRs were synthesized by two-step pulse anodization under voltage control conditions.[56,59] 1.5 x 1.5 cm^2 Al square chips were sonicated in EtOH and ultrapure water for 15 min each, dried under air stream and electropolished in a mixture of EtOH and $HClO_4$ 4:1 (*v*:*v*) at 20 V and 5 °C for 3 min. Anodization was performed in an electrochemical reactor with a circular window 1 cm in diameter. The first anodization step was performed in 0.3 M $H_2C_2O_4$ at 40 V and 6 °C for 20 h. The resulting NAA layer was removed by wet chemical etching in a mixture of 0.2 M H_2CrO_4 and 0.4 M H_3PO_4 at 70 °C for 3 h. The second anodization step was carried out using the same acid electrolyte and temperature as in the first anodization step. The anodization process started with a constant voltage step of 40 V for 10 min. The anodization profile was subsequently switched to pulse mode, in which each asymmetric stepwise pulse consisted of three stages: (i) a high voltage (HV) stage at a constant voltage of 50 V, (ii) a decreasing voltage ramp at a rate of 0.078 Vs^{-1} from 50 V to 20 V, and (iii) a low voltage (LV) stage at a constant voltage of 20 V. The anodization period (T_p) – total time for each pulse – was calculated using **Eq. 1** as the contribution of each pulse stage (i.e. time at HV stage – t_{HV}, time at decreasing ramp stage – $t_{LV\text{-}HV}$, and time at LV stage – t_{LV}). While the number of pulses, $t_{LV\text{-}HV}$ and t_{LV} were fixed at 60 pulses, ~385 s and 8 min, respectively, t_{HV} was systematically modified from 30 to 120 s, with Δt_{HV} = 30 s.

$$T_P = t_{HV} + t_{LV-HV} + t_{LV} \quad (1)$$

The anodization period (T_P) and pore widening time (t_{pw}) were systematically manipulated from 895 to 985 s with ΔT_P = 30 s, and from 0 to 24 min with Δt_{pw} = 12 min, respectively. Note that NAA-DBRs were pore widened in an aqueous solution of 5 wt% H_3PO_4 at 35 °C after fabrication.

The effect of the pore diameter and interpore distance (or lattice constant) on the top surface of NAA-DBRs on the photocatalytic performance of these composite photocatalyst platforms was assessed. The geometric features of NAA-DBRs were systematically modified by a three-step pulse anodization approach, using different starting anodization voltages (V_o) ranged from 60 to 100 V with ΔV_o = 20 V. The first and second anodization steps were performed at V_o using the same acid electrolyte, though the duration of the latter was set to 45, 30 and 15 min for V_o = 60, 80 and 100 V, respectively. After the second anodization step, a pore widening treatment was carried out for 20, 20 and 35 min, respectively, to thin the oxide barrier layer located at the nanopore bottom tips and allow the effective flow of electrolytic species and the translation of anodization voltage modifications into porosity changes. The third anodization step was performed under pulse anodization mode at fixed t_{HV} = 120 s (i.e. T_P = 985 s) (*vide supra*).

Surface Functionalization and Top Coating of NAA-DBRs

The surface of NAA-DBRs was chemically functionalized with layers of photoactive TiO_2 through sol-gel method. EtOH (97 *v*%) and titanium (IV) butoxide (3 *v*%) were mixed under magnetic stirring for 10 min to prepare TiO_2 sol. NAA-DBRs were then immerse in the TiO_2 sol for 24 h to functionalize the inner surface of NAA-DBRs. Surface-functionalized NAA-DBRs were then washed with EtOH to remove any excess of TiO_2 sol and titanium (IV) butoxide. After washing, TiO_2-NAA-DBRs were dried in an oven at 50 °C for 10 min to evaporate residual EtOH. The top surface of TiO_2-NAA-DBRs was subsequently coated with an ultrathin layer of noble metal (i.e. Au or Ag) using a sputter coater equipped with a film thickness monitor (sputter coater 108auto, Cressington, USA). To investigate the effect of surface plasmon resonance (SPR) on the photocatalytic performance of noble metal-TiO_2-NAA-DBRs, the deposition time (τ_D) of noble metal was systematically varied from 0 to 60 s with an interval of $\Delta\tau_D$ = 30 s. The effect of different noble metal coatings (i.e. Au and Ag) was also studied.

Optical Characterization

Prior to optical characterization, the remaining Al substrate was selectively dissolved from the backside of NAA-DBRs by wet chemical etching in a saturated solution of $HCl/CuCl_2$, using an etching cell with a Viton® mask featuring a circular window of 5 mm in diameter. The absorption and transmission spectra of NAA-DBRs fabricated at various conditions were obtained in air and water at normal incidence (i.e. $\theta = 0°$) from 200 to 900 nm with a resolution of 1 nm using a UV–visible–NIR spectrophotometer (Cary 60, Agilent, USA). The absorbance spectrum of 5 mg L^{-1} MB in a 10 mm path length polystyrene cuvette was acquired from 200 to 800 nm to determine the absorbance band of MB (**Fig. S1 – ESI**). The reflection spectra of NAA-DBRs produced with various fabrication conditions at normal incidence were obtained in air and water. The surface of NAA-DBRs was illuminated with white light from a tungsten source (LS-1LL, Ocean Optics, USA) by a bifurcated optical probe. The collection fiber in the optical probe collected and transferred the light reflected from the illumination spot (~2 mm in diameter) to a miniature spectrometer (USB 4000+VIS-NIR-ES, Ocean Optics, USA). The interferometric color displayed by NAA-DBRs as a function of various fabrication parameters was characterized through digital pictures, using a Canon EOS 700D digital camera equipped with a Tamron 90 mm F2.8 VC USD macro mount lens with autofocus function under natural light illumination. The position of the central wavelength of the photonic stopband of NAA-DBRs was estimated by Gaussian fittings in OriginPro 8.5®.

Photocatalytic Degradation of Model Organic

The photocatalytic performance of noble metal-TiO_2-NAA-DBRs produced with different T_P, t_{pw}, τ_D, V_o and noble metal coating was assessed under simulated solar light irradiation conditions using photocatalytic degradation of methylene blue (MB) as an indicator, which is a model organic dye with a well-defined absorbance band within the visible spectral range (i.e. MB – $\lambda_{Abs\text{-}MB}$ = 664 nm). Photocatalytic reactions were performed in a transparent reactor, in which noble metal-TiO_2-NAA-DBRs with an effective area of 1 cm^2 were immersed in a 2 mL solution mixture of 5 mg L^{-1} of MB and 100 mM H_2O_2. The solution was stirred magnetically in a dark vessel (i.e. solar simulator) for 30 min to ensure an adsorption and desorption equilibrium prior to irradiation. The system was then illuminated with a 150 W (~3000 lumen) halogen lamp (HL250-A, Amscope, Australia) at room temperature to simulate solar light., The absorbance of the solution mixture at $\lambda_{Abs\text{-}MB}$ = 664 nm was analyzed for each illumination time interval (i.e. 15 min) by a UV–visible spectrophotometer in order to determine the concentration of MB throughout time. A calibration line establishing the correlation between the absorbance and the concentration of MB was used to obtain the photocatalytic conversion ratio (C_t/C_o), where C_o is the concentration of MB after stirring in the dark for 30 min and C_t is the concentration at a given illumination time t (**Fig. S2 – ESI**). This parameter was used to establish the kinetic model for this photocatalytic system. The average photocatalytic degradation rates were summarized in contour maps generated using OriginPro 8.5® using a triangulation algorithm in which the coordinates of the intersection point were computed with linear interpolation.

Chemical and Structural Characterization

The nanoporous structure of NAA-DBRs produced at various conditions was characterized using a field emission gun scanning electron microscope (FEG-SEM FEI Quanta 450). FEG-SEM images were analyzed by ImageJ to establish the geometric features of NAA-DBRs.[60] The chemical composition of NAA-DBRs before and after surface functionalization with TiO_2 was analyzed by energy dispersive X-ray (EDX) spectroscopy during FEG-SEM characterization.

Results and Discussion

Structural Characterization of NAA-DBRs

Fig. 2 depicts representative FEG-SEM images and a schematic definition of the structural features of NAA-DBRs produced by pulse anodization. NAA-DBRs feature an organized nanoporous geometry in two planar directions: (i) honeycomb-like distribution of nanopores across the top plane, and (ii) periodically modulated nanopore diameter in depth along the normal plane (**Fig. 2a**). The main structural parameters of Au-NAA-DBRs include the total pore length (L_p), interpore distance (d_{int}), pore diameter (d_p), period length (L_{TP}) and noble metal thickness (L_D). **Fig. 2b** shows arrays of homogeneously distributed, hexagonally arranged nanopores across the top surface NAA-DBRs, where the average d_p is 31 ± 4 nm with no pore widening treatment. The cross-sectional view FEG-SEM image displays the constant voltage anodization (CA) step, during which straight cylindrical nanopores are produced (**Fig. 2c**). Alternating stacked layers of NAA with periodic modulation of nanopore diameter are produced during the pulse anodization (PA) stage, as indicated by L_{TP} in the schematic in **Fig. 2a** and the white arrowheads shown in **Fig. 2d**. These periodic layers feature straight cylindrical pores with branched tips that form during high and low voltage anodization stages, respectively. Nanopore branching is associated with the growth of nanopores under non-steady conditions (i.e. low voltage anodization), which is characterized by a current recovery stage in the anodization profile.[53] **Fig. 2e** shows the linear dependence of L_{TP} on T_P, where L_{TP} increases at a rate of 1.00 ± 0.10 nm s^{-1} with T_P. The geometric features (i.e. d_p and d_{int}) of NAA-DBRs also follow a linear trend with V_o, where d_p and d_{int} increase at a rate of 1.94 ± 0.04 and 2.78 ± 0.05 nm s^{-1} with increasing V_o, respectively (**Fig. 2f**).

Effect of Anodization Parameters on the Optical Properties of NAA-DBRs

Fig. 3 presents a representative two-step pulse anodization profile used to produce NAA-DBRs as well as the combined effect of T_P and t_{pw} on the central position of the characteristic photonic stopband (λ_C) of NAA-DBRs in air and water.

View Article Online
DOI: 10.1039/C9CY00627C

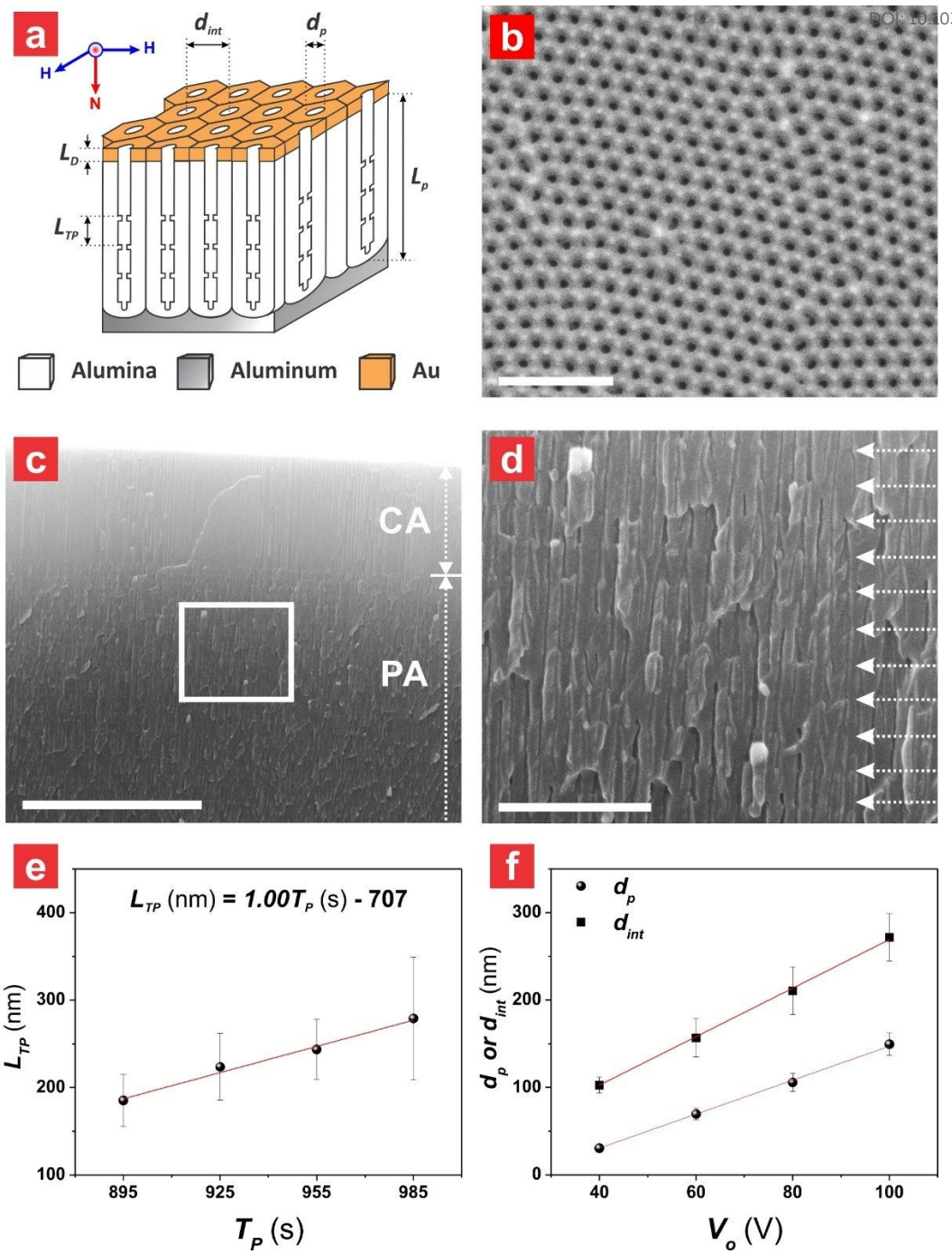

Fig. 2 Nanoporous structure of NAA-DBRs produced by pulse anodization. a) Illustration describing the geometric features of gold-coated NAA-DBRs including the total pore length (L_p), interpore distance (d_{int}), pore diameter (d_p), period length (L_{TP}) and Au thickness (L_D) (note: H = top horizontal plane and N = vertical normal plane). b) Representative top view FEG-SEM image of a NAA-DBR produced by two-step pulse anodization with anodization period T_P = 985 s, number of anodization pulses N_p = 60 pulses and pore widening time t_{pw} = 0 min (scale bar = 500 nm). c) General cross-sectional view FEG-SEM image of a NAA-DBR, where CA and PA represent the constant (CA) and pulse voltage anodization (PA) steps (scale bar = 5 µm). d) Magnified view of the white square shown in c) (scale bar = 1 µm). e) Linear correlation establishing the dependency of L_{TP} and T_P from 895 to 985 s. f) Linear dependence of d_{int} and d_p on the voltage during the constant anodization step (V_o).

The anodization profile demonstrates that current density (i.e. output) follows the pulse anodization voltage (i.e. input) applied during the second anodization step (**Fig. 3a**). However, a slight current recovery period was observed as compared to NAA-DBRs fabricated in H_2SO_4 electrolyte.[11,47] This is due to the thicker oxide barrier layer located at the nanopore bottom tips under these fabrication conditions.[61] To understand the effect of T_P and t_{pw} on the optical properties of NAA-DBRs, a set of NAA-DBRs was produced by systematically modifying T_P from 895 to 985 s with ΔT_P = 30 s, and t_{pw} from 0 to 24 min with Δt_{pw} = 12 min. **Fig. 3b** depicts the interferometric color displayed by these photonic crystal structures in air, where some NAA-DBRs

display vivid color from purplish blue to red, while others display transparent color (i.e. black background). The position of the characteristic PSB dictates the interferometric color displayed by the NAA-DBRs. As such, these PCs feature transparent and vivid colors when the characteristic photonic stopband (PSB) falls within the NIR and visible regions of the spectrum, respectively (**Fig. S3 – ESI**). The intensity of the characteristic PSB also plays a major role in the intensity of the interferometric color of NAA-DBRs. For instance, NAA-DBRs produced with T_P = 895 and 955 s at t_{pw} = 0 min display weak green and red colors, respectively, as compared to the vivid colors shown by their analogue NAA-DBRs produced at t_{pw} = 12 min (i.e. intense blue and red, respectively). Digital images also demonstrate that the interferometric color of NAA-DBRs red-shifts with increasing T_P. For example, NAA-DBRs produced with T_P = 895, 925, 955 and 985 s at t_{pw} = 24 min show vivid blue, green, orange and red color, respectively. In contrast to the effect of T_P, the interferometric color of NAA-DBRs blue-shifts with t_{pw}, as revealed by the red, gold and green vivid colors observed for NAA-DBRs fabricated at T_P = 925 s with increasing t_{pw}, from 0 to 24 min with Δt_{pw} = 12 min, respectively. The correlation between T_P and λ_C establishes a linear relationship with t_{pw} from 0 to 24 min, where the slopes of the linear fittings were 3.59 ± 0.09, 3.54 ± 0.03 and 3.22 ± 0.09 nm s^{-1}, respectively (**Fig. 3c**). λ_C can be tuned from 421 ± 1 nm (T_P = 895 s and t_{pw} = 6 min) to 854 ± 1 nm (T_P = 985 s and t_{pw} = 0 min) for the range of anodization parameters studied, demonstrating that λ_C red-shifts with increasing T_P and blue-shifts with increasing t_{pw}. The optical properties of NAA-DBRs were characterized in water to identify photocatalytic enhancements associated with "slow photon" effect, since the photocatalytic degradation of MB was performed in aqueous solution. **Fig. 3d** shows the linear dependence of λ_C on T_P in water, in which the former parameter red-shifts at a rate of 3.26 ± 0.08, 3.44 ± 0.23 and 3.42 ± 0.10 nm s^{-1} with the latter parameter for t_{pw} = 0, 12 and 24 min, respectively. These results also demonstrate that λ_C blue-shifts with increasing t_{pw}. The position of the characteristic PSB of NAA-DBRs in water can be tuned from 483 ± 1 nm (T_P = 895 s and t_{pw} = 6 min) to 887 ± 1 nm (T_P = 985 s and t_{pw} = 0 min), as denoted in the transmission spectra shown in **Fig. S4** (**ESI**). When the medium filling the nanoporous structures of NAA-DBRs is changed from air to water, the position of the characteristic PSB is red-shifted at an average rate of 46 ± 17, 42 ± 14 and 80 ± 13 nm s^{-1} for t_{pw} = 0, 12 and 24 min, respectively (**Figs. 3c** and **d**). These red-shifts are associated with the filling of nanoporous network of NAA-DBRs with a medium of higher refractive index than that of air (i.e. n_{air} = 1.00 RIU and n_{water} = 1.33 RIU). These results demonstrate that the optical characteristics of NAA-DBRs can be precisely tuned across the visible–NIR spectrum by systematically manipulating the fabrication parameters (i.e. T_P and t_{pw}).

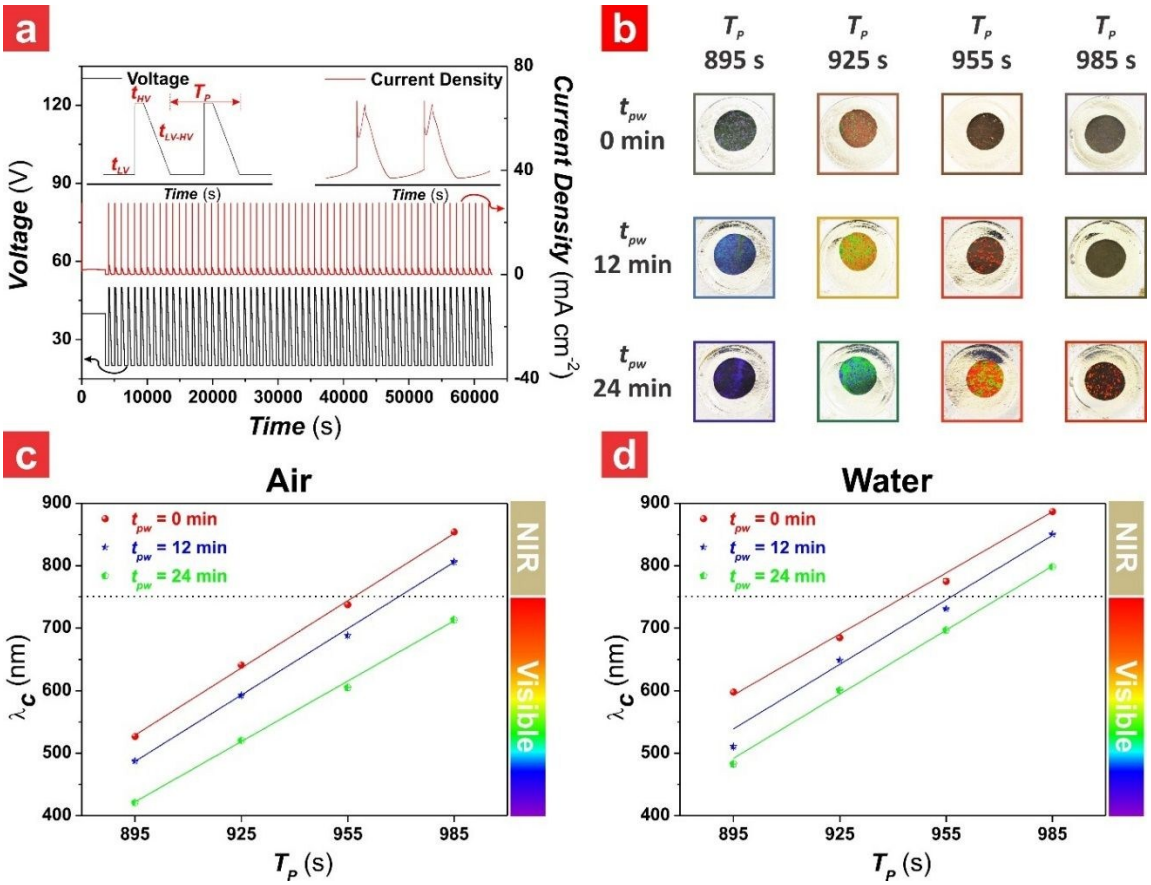

Fig. 3 Effect of anodization period (T_P) and pore widening time (t_{pw}) on the optical properties of NAA-DBRs. a) Representative anodization profile of NAA-DBRs produced by pulse anodization with T_P = 985 s and N_p = 60 pulses. b) Digital pictures of NAA-DBRs produced with different T_P and t_{pw} values. c) and d) Central position of the characteristic photonic stopband (PSB – λ_C) as a function of T_P and t_{pw}, where the medium filling the nanoporous structure of NAA-DBRs is air and water, respectively.

View Article Online
DOI: 10.1039/C9CY00627C

Catalysis Science & Technology

ARTICLE

Effect of Surface Functionalization of TiO_2 and Noble Metal Coating on the Properties of NAA-DBRs

Fig. 4 depicts the effect of the deposition of TiO_2 layers and noble metal (i.e. Au) on the chemical and optical characteristics of NAA-DBRs. Photoactive layers of TiO_2 were deposited onto the inner surface of NAA-DBRs by sol-gel method to develop a photoactive composite photonic crystal structure for photocatalysis.

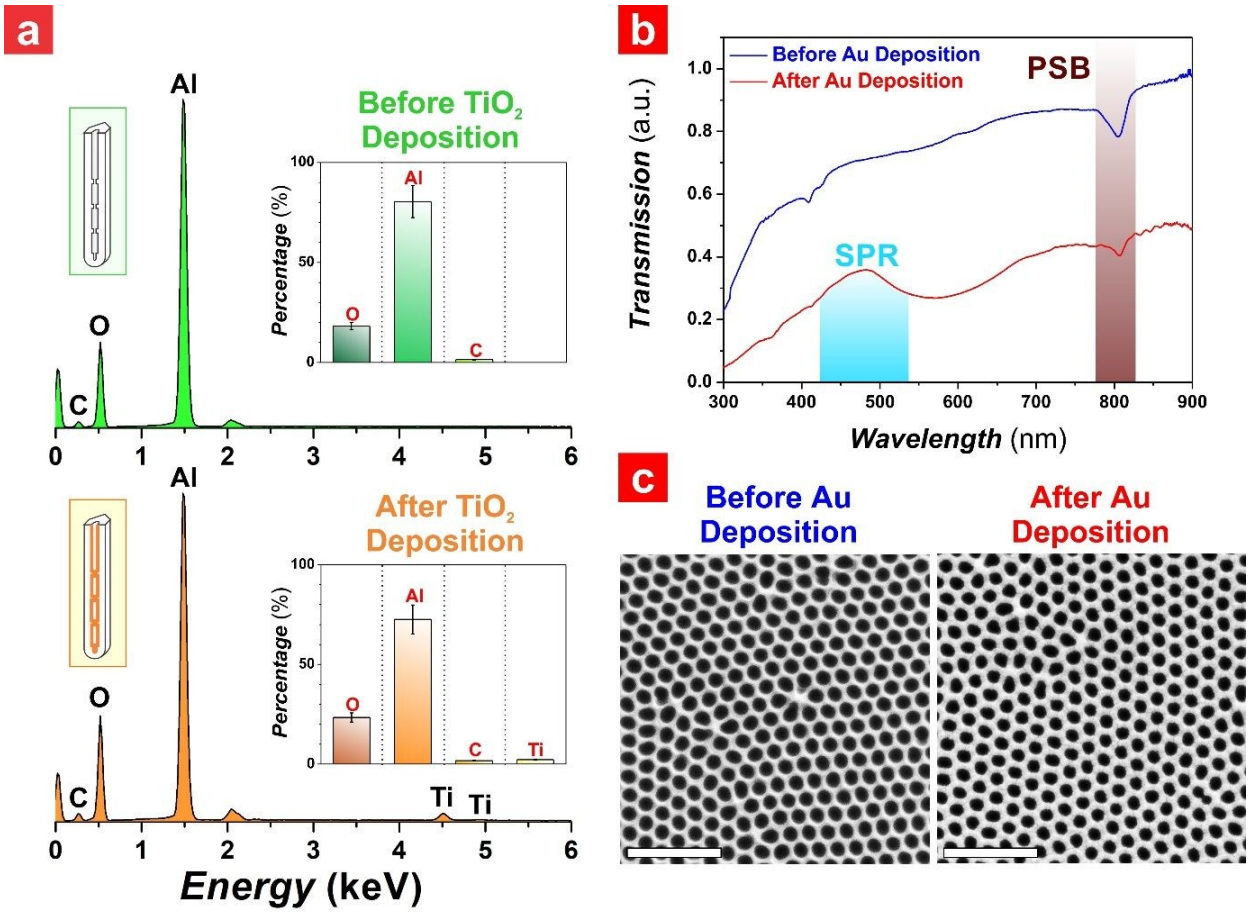

Fig. 4 Chemical and optical characterization of Au-TiO_2-NAA-DBRs after surface functionalization with photoactive layers of TiO_2 and top coating with metallic Au. a) Energy dispersive X-ray (EDX) spectra of a representative NAA-DBR with insets showing the schematic composition of NAA-DBRs (left) and the percentage of main elements present (right) before and after surface functionalization with TiO_2 (note: NAA-DBR produced with T_p = 985 s and t_{pw} = 24 min). b) Transmission spectrum of the representative NAA-DBR in water showing the surface plasmon resonance band (SPR) and characteristic photonic stopband (PSB) before and after coating the top surface with Au for a deposition time (τ_D) of 30 s. c) FEG-SEM images of the representative NAA-DBR from (b) before and after Au coating (scale bar = 500 nm).

Fig. 4a shows the energy dispersive X-ray (EDX) spectra, including insets of graphical illustration of NAA-DBRs (left) and percentage of main elements (right), before and after depositing TiO_2 onto the inner surface of NAA-DBRs. The EDX spectrum for as-produced NAA-DBRs indicates that the percentage of elements such as Al, O and C were 80.4 ± 8.0, 18.2 ± 1.8 and 1.4 ± 0.1 %, respectively. These atoms correspond to the chemical composition of the photonic structures, where Al and O atoms correspond to alumina (Al_2O_3) and C atoms are associated with contaminants incorporated into the alumina structure from the acid electrolyte (i.e. oxalic acid) during anodization. After surface functionalization with TiO_2 layers, the percentages of Al, O, C and Ti were determined to be 72.6 ± 7.3, 23.4 ± 2.3, 1.7 ± 0.2 and 2.3 ± 0.2 %, respectively. The relative percentage increment in the characteristic peaks of O and Ti atoms after TiO_2 deposition indicates that photoactive TiO_2 layers were successfully deposited onto the inner surface of NAA-DBRs. The top surface of NAA-DBRs was also coated with thin layers of Au by sputtering to provide the surface plasmon resonance

View Article Online
DOI: 10.1039/C9CY00627C

(SPR) in the composite photonic crystal structures. **Fig. 4b** shows transmission spectra of a representative NAA-DBR in water before and after coating with a thin film of Au for 30 s. Before coating, the position of the characteristic PSB is located at 804 ± 1 nm. After Au coating for 30 s (L_D = 5 ± 1 nm), a less intense characteristic PSB is observed at 806 ± 1 nm, which is statistically the same as that of the as-produced NAA-DBR. This suggests that incorporation of Au does not shift the PSB of NAA-DBRs and slow photons still exist in these PC structures. This observation is in good agreement with previous studies.[7] However, an extraordinary optical transmission band due to surface plasmon resonance (λ_{SPR}) is observed at 481 ± 1 nm in Au-coated NAA-DBRs, which corresponds to the characteristic SPR band of Au. The successful deposition of a thin film of Au is further supported by the representative top view FEG-SEM images shown in **Fig. 4c**, in which the pore diameter (d_p) in a NAA-DBR at t_{pw} = 24 min is reduced from 81 ± 6 to 70 ± 4 nm after Au deposition. However, Au-TiO_2-NAA-DBRs maintain their original morphology after Au deposition (**Fig. S5 – ESI**). XRD spectra also successfully demonstrate the deposition of TiO_2 and Au, where the three characteristic peaks corresponding to an amorphous alumina (Al_2O_3) phase in XRD spectra of as-produced NAA-DBRs (i.e. 45°, 65° and 78°) undergoes a slight shift and decrease in intensity after surface functionalization of TiO_2 followed by Au coating (**Fig. S6 – ESI**). A weak characteristic peak corresponding to polycrystalline Au in the XRD spectrum of Au-TiO_2-NAA-DBRs (i.e. 39°) is also observed. This indicates that, while TiO_2 layers are crystallographically amorphous, the deposited Au film is polycrystalline. The successful deposition of Au and TiO_2 layers on NAA-DBRs were further characterized by FEG-SEM image analysis, contact angle and EDX spectra (**Fig. S7 – ESI**).

As these results demonstrate, Au-TiO_2-NAA-DBRs are ideal model platforms to integrate and engineer slow photons and surface plasmon resonances. SPR modes are characterized by an extraordinary transmission band (λ_{SPR}) that can be controlled by modifying the geometric features of nanopores (i.e. d_p, d_{int} and L_D) at the top plane of NAA-DBRs (horizontal plane). The Bragg modes (i.e. slow photons), characterized by the PSB, can be tuned by modifying the period length (L_{TP}) along the normal plane of the NAA-DBR structure. These versatile hybrid plasmonic–photonic crystal structure enables the engineering of photocatalytic enhancements by coupling between slow photon and SPR effects.

Assessment of Photocatalytic Degradation of MB by Au-TiO_2-NAA-DBRs

The photocatalytic performance of Au-TiO_2-NAA-DBRs was analyzed by monitoring the degradation of MB molecules under visible–NIR irradiation. The absorbance maximum of MB ($\lambda_{Abs\text{-}MB}$) is located at 664 nm (**Fig. S1 – ESI**). The concentration of this organic dye at a given illumination time t (C_t) was estimated from a previously established calibration line (**Fig. S2 – ESI**). The photocatalytic performance of the hybrid plasmonic–photonic crystal structures was fitted to the linearized pseudo-first order kinetics model shown in **Eq. 2**:

$$-\ln(C_t/C_o) = kt \quad (2)$$

where C_o is the concentration at adsorption and desorption equilibrium and k is the kinetic constant.

Photocatalytic degradation of MB was carried out with 100 mM H_2O_2 solution to provide photogeneration of additional charge carriers from the relatively thin photoactive TiO_2 layer in Au-TiO_2-NAA-DBRs. The simulated solar light irradiation used in our study has a spectral distribution of 0.12 % UV (350–400 nm), 64.60 % visible (400–750 nm) and 35.28 % NIR (800–1025 nm). Therefore, these photocatalytic reactions were mostly driven by visible–NIR irradiation (**Fig. S8 – ESI**).

Effect of Fabrication Parameters of Au-TiO_2-NAA-DBRs on the Photocatalytic Degradation of MB

NAA-DBRs are 1D photonic crystals with a well-defined PSB that can be precisely tuned across the spectral regions by modifying the anodization parameters. Functionalization of the inner surface of NAA-DBRs with TiO_2 layers provides these nanoporous PCs with essential photocatalytic activity to photodegrade organic molecules. However, these composite semiconductor PCs also provide opportunities to further enhance the efficiency of photocatalytic reactions by engineered "slow photon" effect. Slow photons have reduced group velocity at those spectral regions near the blue and red edges of the characteristic PSB.[62] This effect enhances photon-to-electron conversion rate since photons have longer lifespan within the composite photonic structures. The top surface of TiO_2-NAA-DBRs can also be coated with thin films of noble metals to further enhance the photocatalytic performance of the composite platform by SPR, which minimizes the recombination rate of electron/hole pairs at the hybrid heterojunction Au-TiO_2-NAA-DBRs, and extends the absorption of visible light by the hybrid plasmonic–photonic crystal structure.[5] Photocatalytic degradation of methylene blue was analyzed under simulated solar light irradiation as indicator to identify photocatalytic enhancements associated with coupling effects between slow photons and SPR in Au-TiO_2-NAA-DBRs. The anodization period (T_P), pore widening time (t_{pw}) and Au deposition time (τ_D) of Au-TiO_2-NAA-DBRs were systematically modified from T_P = 895 to 985 s with ΔT_P = 30 s, from t_{pw} = 0 to 24 min with Δt_{pw} = 12 min, and from τ_D = 0 to 60 s with $\Delta\tau_D$ = 30 s, respectively. **Fig. 5** depicts the linearized pseudo-first order kinetics for the photocatalytic degradation of MB by Au-TiO_2-NAA-DBRs (t_{pw} = 0 min) with different T_P and τ_D, where the slope corresponds to the kinetic constant (k) or the photocatalytic performance of Au-TiO_2-NAA-DBRs. The obtained results for Au-TiO_2-NAA-DBRs with t_{pw} = 12 and 24 min are provided in **Figs. S9** and **S10** (**ESI**), respectively. A summary of the k values obtained from linear fittings of these linearized pseudo-first order photodegradation kinetics of MB is provided in **Table S1** (**ESI**) and **Fig. 6**. **Figs. 6a-c** illustrate contour maps summarizing the effect of T_P and τ_D on k values for Au-TiO_2-NAA-DBRs produced with t_{pw} = 0, 12 and 24 min, respectively, and **Figs. 6d-f** depict the correlation between the

View Article Online
DOI: 10.1039/C9CY00627C

absorbance band of MB and the position of the blue and red edges of the characteristic PSB of Au-TiO_2-NAA-DBRs fabricated with t_{pw} = 0, 12 and 24 min, respectively.

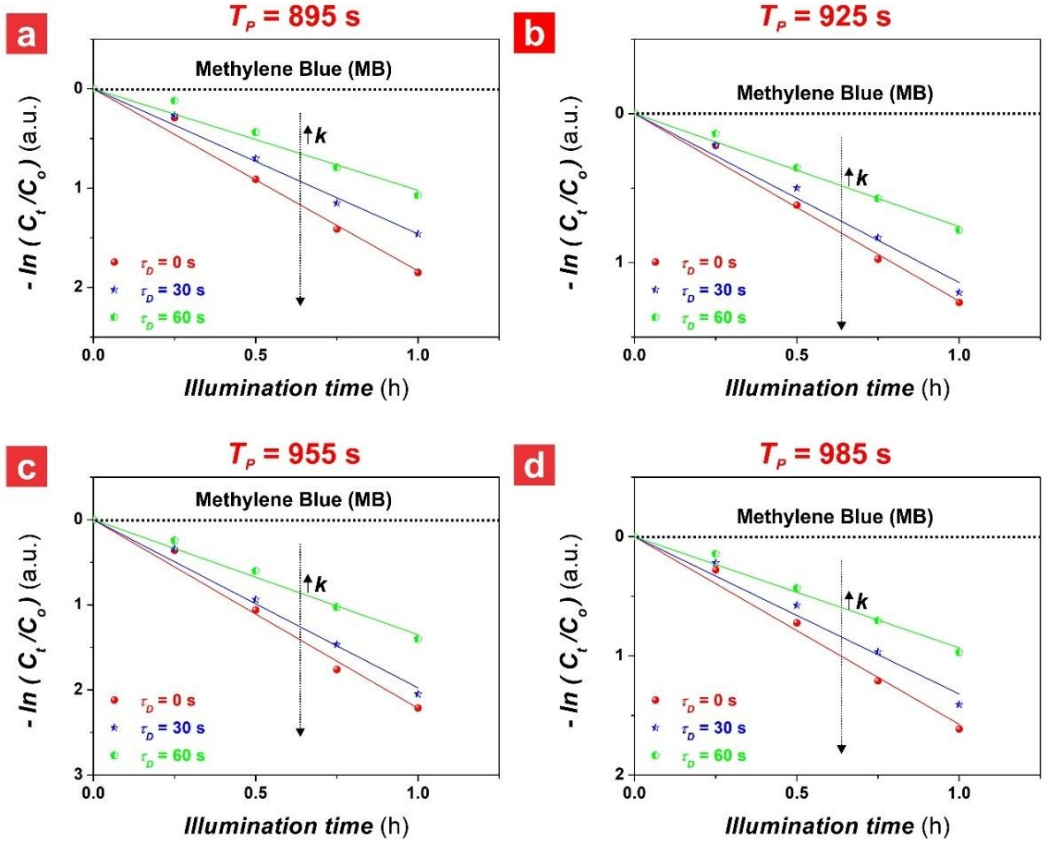

Fig. 5 Photocatalytic degradation kinetics of methylene blue (MB) by Au-TiO_2-NAA-DBRs fabricated by two-step pulse anodization at fixed pore widening time (t_{pw} = 0 min), and variable Au deposition time (τ_D = 0, 30 and 60 s) and anodization period (T_P = a) 895 s, b) 925 s, c) 955 s and d) 985 s) under controlled irradiation conditions (note: black dotted lines correspond to the photodegradation of MB in control NAA-DBRs without photoactive TiO_2 layer).

Fig. 6a shows a homogenous bimodal dependency of k on T_P and τ_D, as indicated by the equidistant color field lines with T_P and τ_D and the two local maxima of k at T_P = 895 s and τ_D = 0 s, and at T_P = 955 s and τ_D = 0 s. When τ_D is fixed at 0 s (i.e. no SPR in the composite PC structures), k decreases from T_P = 895 to 925 s (i.e. from k = 1.83 ± 0.06 to 1.26 ± 0.04 h^{-1}), increases to a maximum of kinetic constant at T_P = 955 s (i.e. k_{max} = 2.22 ± 0.08 h^{-1}), and it decreases again to a lower k value at T_P = 985 s (i.e. k = 1.57 ± 0.05 h^{-1}). These results denote that at τ_D = 0 s, Au-TiO_2-NAA-DBRs produced with T_P = 955 s photodegrade MB molecules more efficiently than their counterparts produced at different anodization periods. This result can be correlated with the relative position of the edges of characteristic PSB and the absorbance band of MB (**Fig. 6b**). Au-TiO_2-NAA-DBRs produced with T_P = 955 s achieve the highest k value since the characteristic PSB of these PCs partially overlaps the absorbance band of MB, with the PSB's blue edge located ~89 nm away from the absorbance maximum of MB (i.e. $\lambda_{Abs\text{-}MB}$ = 664 nm). On the other hand, Au-TiO_2-NAA-DBRs fabricated with T_P = 925 s show the lowest k value, where the distance between the PSB's blue edge and the absorbance maximum of MB is the shortest (i.e. ~22 nm). The relative position between the red and blue edges of the characteristic PSB and the absorbance band of the model organic are critical in enhancing light–matter interactions and boosting photon-to-electron conversion rates. The photocatalytic performance of Au-TiO_2-NAA-DBRs is significantly enhanced when the edges of the characteristic PSB partially overlap with the absorbance band of MB.[10,62-65] However, when the edges of the PSB fall within the absorbance maximum of MB or are too far from the absorbance band of MB (T_P = 925 and 985 s), the photocatalytic performance is reduced significantly. The poor photocatalytic performance observed for Au-TiO_2-NAA-DBRs produced with T_P = 925 s is attributed to the screening effect by MB molecules at their maximum of absorbance (i.e. $\lambda_{Abs\text{-}MB}$ = 664 nm; ~2.9 a.u.). Under such configuration, most of the irradiated light is absorbed by MB molecules before it reaches the inner surface of the composite PC structures. This dramatically reduces the photocatalytic efficiency of Au-TiO_2-NAA-DBRs due to the poor utilization of incoming photons by the photoactive TiO_2 layer. This observation is in good agreement with previous studies.[10] It is worth noting that the characteristic PSB of the second best performing Au-TiO_2-NAA-DBR structure (T_P = 895 s) is also partially overlapped with the absorbance band of MB, though with a reasonable distance between the PSB's red edge and the absorbance maximum of MB (i.e. ~ 36 nm). Where a characteristic PSB is completely outside of the absorbance band of MB, the photocatalytic degradation rate of Au-TiO_2-NAA-DBR is strongly dependent on the geometric features of the nanoporous PC structures

and independent on the "slow photon" effect. The main geometric factor affecting the photocatalytic performance of Au-TiO_2-NAA-DBRs in this situation is the total pore length (L_P), which is directly proportional to the anodization time.[10,66,67] The overall light absorption of the composite PC structure enhances with increasing L_P, leading to an increase in the photogeneration of charge carriers and the overall photodegradation rate achieved by Au-TiO_2-NAA-DBRs. Au-TiO_2-NAA-DBRs produced with T_P = 985 s have the longest pore length (i.e. total anodization time = 17.4 h) as compared to their analogues fabricated with shorter T_P (i.e. from 15.9 to 16.9 h). In summary, this analysis reveals that the photocatalytic performance of Au-TiO_2-NAA-DBRs produced with t_{pw} = 0 min, τ_D = 0 s and varying T_P follows the order 955 > 895 > 985 > 925 s.

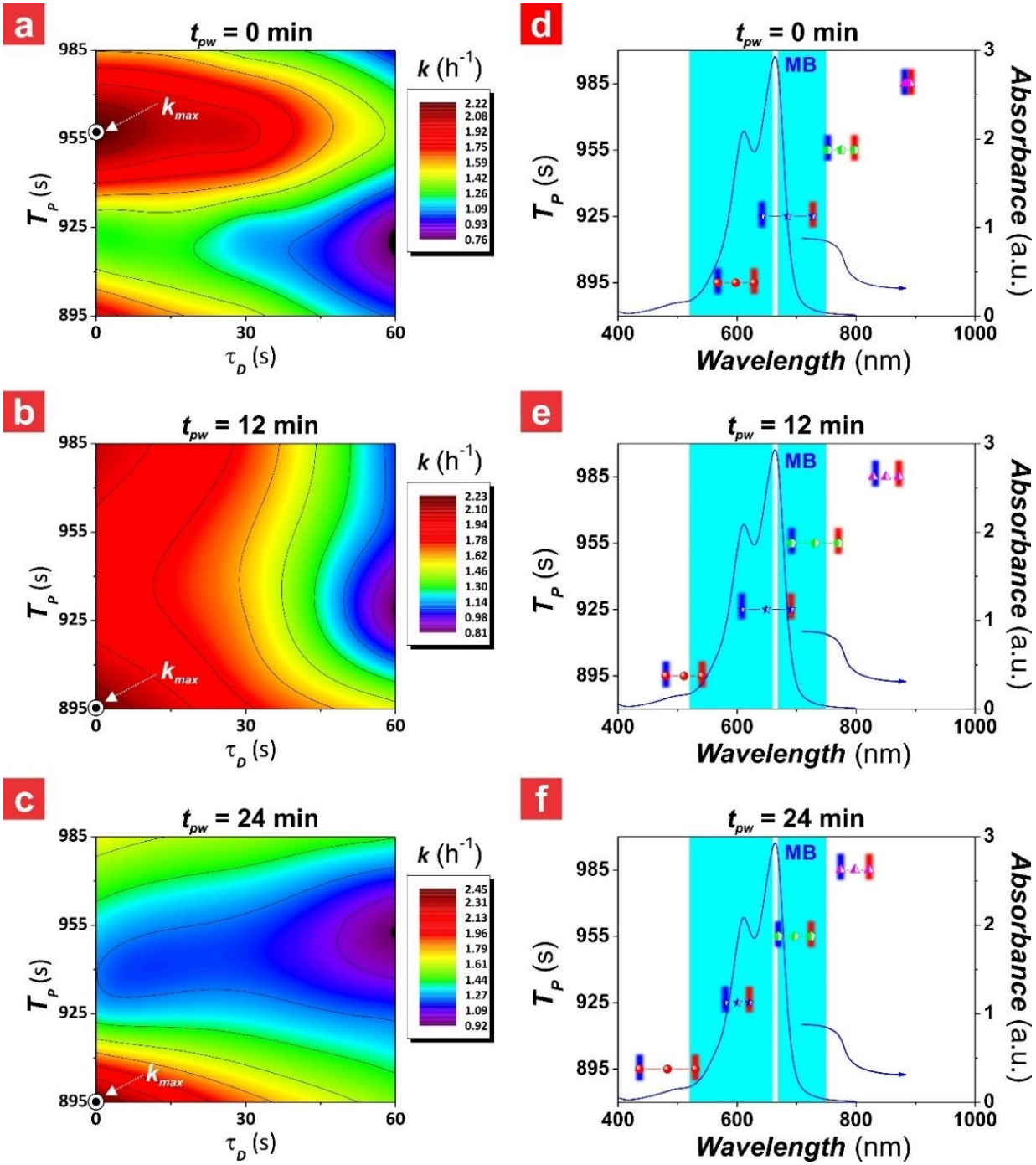

Fig. 6 Combinational effect of anodization period (T_P), pore widening time (t_{pw}), Au deposition time (τ_D) and position of the blue and red edges of characteristic stopband (PSB) of Au-TiO_2-NAA-DBRs on the photocatalytic degradation rates (k) of methylene blue (MB). a-c) Contour plots showing the combined effect of T_P and τ_D on k values for the photodegradation of MB by Au-TiO_2-NAA-DBRs with t_{pw} = 0, 12 and 24 min, respectively. d-f) Relative position of the blue and red edges of the characteristic PSB of Au-TiO_2-NAA-DBRs produced with varying T_P from 895 to 985 s with ΔT_P = 30 s with respect to the absorbance band of MB for t_{pw} = 0, 12 and 24 min, respectively (note: white gap inside the absorbance band of MB denotes the absorbance maximum of MB – $\lambda_{abs\text{-}MB}$ = 664 nm, while the blue and red vertical lines on the PSB correspond to the blue and red edges of the PSB).

View Article Online
DOI: 10.1039/C9CY00627C

Catalysis Science & Technology

ARTICLE

Fig. 6a shows that this trend is consistent with increasing thickness of the Au coating (from τ_D = 0 to 60 s) in Au-TiO_2-NAA-DBRs produced at t_{pw} = 0 min. However, these hybrid plasmonic–photonic crystal structures achieve lower k values in general, as indicated by the color field distribution with increasing τ_D. The minimum kinetic constant (k_{min}) of 0.76 ± 0.02 h^{-1} is achieved by those Au-TiO_2-NAA-DBRs fabricated with T_P = 925 s and τ_D = 60 s (i.e. black region of the contour map), denoting that the k values decrease with increasing τ_D. This phenomenon can be explained by analyzing the optical characteristics of Au-TiO_2-NAA-DBRs as a function of τ_D. The optical behavior of Au-TiO_2-NAA-DBRs is equivalent to the sum of their transmission, absorption and reflection. To gain further insight into the effect of τ_D on the photocatalytic behavior of Au-TiO_2-NAA-DBRs, we analyzed the optical transmission, absorption and reflection of a representative Au-TiO_2-NAA-DBR produced with T_P = 925 s, t_{pw} = 24 min and medium = air (**Fig. 7**). The transmission spectrum of these hybrid plasmonic–photonic crystal structures show a characteristic SPR band at 491 ± 1 nm for Au-TiO_2-NAA-DBRs synthesized with τ_D = 30 and 60 s (**Fig. 7a**). This SPR band results from an extraordinary transmission of light and can be controlled by modifying the geometric features of the nanopores on the top surface of the hybrid plasmonic–photonic crystal structures. However, as the orange shaded region in the transmission spectra indicates, the deposition of a thin layer of gold on the top surface of TiO_2-NAA-DBR reduces the intensity of the characteristic PSB with increasing τ_D, and also red-shifts slightly its position from 612 ± 1 to 615 ± 1 nm when τ_D is increased from 0 to 60 s. The absorption spectra at different τ_D (**Fig. 7b**) confirms that the position of the characteristic PSB is slightly red-shifted with increasing τ_D. Though the intensity of the characteristic PSB is similar in all the cases, the overall light absorption by the composite PC structure increases significantly with increasing τ_D. **Fig. 7c** demonstrates that the intensity of the characteristic PSB in the reflection spectrum decreases with increasing τ_D, while its position remains practically constant (only a slight red shift is observed, from 612 ± 1 to 613 ± 1 nm when τ_D is increased from 0 to 60 s). The effect of the deposition of the thin Au layer can also be observed in the interferometric color of the Au-TiO_2-NAA-DBR, which switches from red to gold color with increasing τ_D. This analysis indicates that transmission and reflection of Au-TiO_2-NAA-DBRs decrease with increasing τ_D, while their optical absorption increases. As the k values reveal, Au-TiO_2-NAA-DBRs have a poorer photocatalytic performance with increasing τ_D. This observation is attributable to the light screening effect by the thin Au layer deposited on the top surface of TiO_2-NAA-DBRs, which reduces the amount of incident photons that travel across the bulk photocatalyst platforms. The localized position of the Au thin film on the top surface of Au-TiO_2-NAA-DBRs implies that no effective Schottky barrier is formed between the Au nanostructure and the functional TiO_2 layer deposited onto the inner surface of TiO_2-NAA-DBRs. The absence of an effective hybrid heterojunction between Au and TiO_2 and the absorption of light by the Au film prevents the effective transfer of photo-excited electrons from the Au layer to the semiconductor layers and the photogenerated carriers are mainly recombined in the Au layer, worsening the overall photocatalytic degradation of MB molecules by Au-TiO_2-NAA-DBRs.

Fig. 6b shows a k maximum of 2.23 ± 0.08 h^{-1} at T_P = 895 s and τ_D = 0 s, and a minimum of 0.82 ± 0.03 h^{-1} at T_P = 925 s and τ_D = 60 s for Au-TiO_2-NAA-DBRs fabricated with t_{pw} = 12 min. The contour map reveals a smooth variation of k with T_P and τ_D, as indicated by the homogeneous distribution of color fields. However, the effect of T_P on the photocatalytic performance of Au-TiO_2-NAA-DBRs is less significant than that of τ_D at t_{pw} = 12 min. The dependence of k with τ_D is stronger at longer deposition times, as indicated by the denser distribution of color fields and field lines with increasing τ_D. The photocatalytic performance of Au-TiO_2-NAA-DBRs decreases with increasing τ_D, which is in good agreement with the results obtained for Au-TiO_2-NAA-DBRs fabricated with t_{pw} = 0 min. The photocatalytic performance of Au-TiO_2-NAA-DBRs (t_{pw} = 12 min) is strongly dependent on the relative position between the edges of the characteristic PSB and the absorbance band of MB molecules (**Fig. 6e**). The photocatalytic enhancement associated with "slow photon" effect is apparent when the characteristic PSB partially overlaps the absorbance band of MB. Au-TiO_2-NAA-DBRs produced with T_P = 895 s achieve the k_{max} since more than half of the characteristic PSB is located outside of the absorbance maximum of MB (i.e. ~123 nm away). In contrast, Au-TiO_2-NAA-DBR fabricated with T_P = 925 s provide the worst k since the characteristic PSB of PCs is located under the maximum of absorbance of MB (i.e. PBS's blue edge ~27 nm away from $\lambda_{Abs\text{-}MB}$ = 664 nm). The characteristic PSB of Au-TiO_2-NAA-DBRs fabricated with T_P = 985 s is entirely outside of the absorbance band of MB. Under that configuration, the photocatalytic performance of these composite PCs relies exclusively on the total length of the nanopores. These Au-TiO_2-NAA-DBRs show slightly superior performance than that of their counterparts fabricated with T_P = 925 and 955 s at any τ_D = 0, 30 and 60 s, respectively. Hence, the photodegradation rate of MB in Au-TiO_2-NAA-DBRs produced with t_{pw} = 12 min follows the order follows T_P = 895 > 985 > 955 > 925 s.

View Article Online
DOI: 10.1039/C9CY00627C

Catalysis Science & Technology

ARTICLE

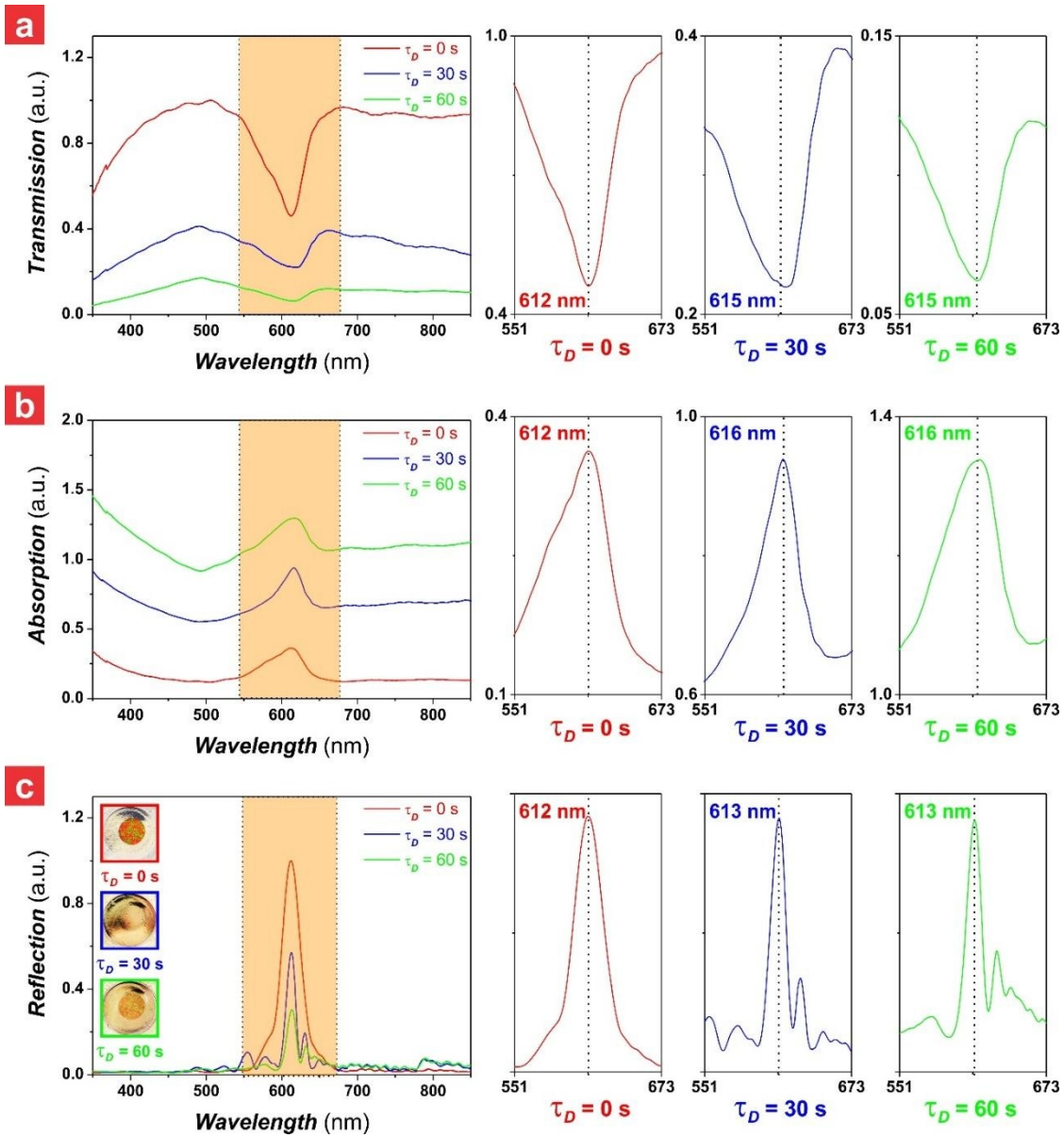

Fig. 7 Optical characterization of a representative Au-TiO_2-NAA-DBRs produced with anodization period T_P = 955 s and pore widening time t_{pw} = 24 min in air (note: shaded regions correspond to the magnified views of the photonic stopbands (PSB) for different τ_D shown on the right side). a) Transmission spectrum of the Au-TiO_2-NAA-DBRs as a function of the Au deposition time (τ_D). b) Absorption spectrum of the Au-TiO_2-NAA-DBRs as a function of τ_D. c) Reflection spectrum and digital pictures of the Au-TiO_2-NAA-DBRs as a function of τ_D.

Fig. 6c summarizes the photocatalytic performance of Au-TiO_2-NAA-DBRs fabricated with t_{pw} = 24 min as a function of T_P and τ_D. As the contour map shows, k_{max} (i.e. 2.45 ± 0.13 h^{-1}) and k_{min} (i.e. 0.92 ± 0.03 h^{-1}) are located at T_P = 895 s and τ_D = 0 s, and T_P = 955 s and τ_D = 60 s, respectively. The distribution of color fields and field lines is denser within the area around the local maximum, for T_P < 925 s and τ_D < 30 s, indicating a strong dependence of k on these fabrication conditions. However, at T_P > 925 s, the kinetic constant becomes less dependent on τ_D as indicated by the broad color fields and field lines. The k values decrease with increasing τ_D and the photocatalytic performance of these Au-TiO_2-NAA-DBRs follows the order T_P =

895 > 985 > 955 > 925 s. This behavior is analogue to that of Au-TiO_2-NAA-DBRs produced at different pore widening times, though the overall *k* values are slightly higher than those of their counterparts produced at t_{pw} = 0 and 12 min. The photocatalytic performance order of Au-TiO_2-NAA-DBRs fabricated at t_{pw} = 24 min is dictated by the relative position of the characteristic PSB of these composite PC structures with respect to the absorbance band of MB (**Fig. 6f**). The "slow photon" effect significantly enhances the photodegradation of MB when the characteristic PSB partially falls within the absorbance band of MB and its edges are positioned far away from the absorbance maximum of MB. As **Fig. 6f** shows, Au-TiO_2-NAA-DBRs fabricated with T_P = 895 s achieve k_{max} = 2.45 ± 0.13 h^{-1}, the characteristic PSB of these Au-TiO_2-NAA-DBRs is slightly overlapped with the absorbance band of MB, with the PSB's red edge located far away from the maximum of absorbance of MB (i.e. ~134 nm away). When the distance between the maximum of absorbance of MB and the blue edge of the PSB of these Au-TiO_2-NAA-DBRs is the narrowest (i.e. ~5 nm for Au-TiO_2-NAA-DBRs produced with T_P = 955 s), the photocatalytic performance is the worst as compared to that of Au-TiO_2-NAA-DBRs produced with shorter anodization period (i.e. T_P = 895 and 925 s). This result is attributable to the light screening effect by MB molecules at those spectral regions near the absorbance maximum of MB. It is noteworthy that Au-TiO_2-NAA-DBRs fabricated with T_P = 985 s show a photocatalytic behavior that is independent on the "slow photon" effect since the PSB is located far away from the absorbance band of MB. Under this configuration, the photocatalytic performance of these Au-TiO_2-NAA-DBRs relies strongly on the total pore length, achieving the second best performance at any τ_D.

To summarize, **Figs. 6a-c** show that Au-TiO_2-NAA-DBRs fabricated with t_{pw} = 24 min provide the highest k_{max} and k_{min} values. These k_{max} and k_{min} were found to be 8–9% and 12–17% higher than those of Au-TiO_2-NAA-DBRs produced with shorter t_{pw}. The superior performance achieved by Au-TiO_2-NAA-DBRs at t_{pw} = 24 min can be associated with the broader and more intense characteristic PSB of these composite PCs, which provides a more efficient collection and utilization of incident photons to photodegrade MB molecules. An enhancement in photocatalytic degradation of MB in Au-TiO_2-NAA-DBRs is strongly dependent on the "slow photon" effect. This enhancement is apparent when the edges of the characteristic PSB of these composite PCs partially overlap the absorbance band of MB, though they are positioned far away from the absorbance maximum of MB. When the vicinity of the characteristic PSB is near the maximum of absorbance of MB, the photocatalytic performance of Au-TiO_2-NAA-DBRs is significantly reduced due to light screening effect (i.e. MB molecules absorb light efficiently in these spectral regions so incoming photons cannot reach the photoactive layers within the nanoporous PC structure). When the characteristic PSB of Au-TiO_2-NAA-DBRs is located completely outside of the absorbance band of MB, the photocatalytic performance relies exclusively on the geometric features of the nanoporous PC and are independent on the "slow photon" effect. Our study also indicates that, while incorporation of a nanoporous plasmonic structure enhances the overall collection of incident photons in Au-TiO_2-NAA-DBRs, this is not translated into an effective utilization of SPR photons in the photocatalytic reaction. This is due to the isolated position of the Au film on the top surface of the PC structure. Incident light is partially absorbed by the Au film to generate SPR photons, minimizing the amount of incoming photons that travel across the PC structure. SPR photons are localized onto the top surface of the PC structure and cannot be efficiently transferred into the TiO_2 photoactive layer on the inner surface of Au-TiO_2-NAA-DBRs. As a result, the incorporation of the Au film worsens the photocatalytic performance of Au-TiO_2-NAA-DBRs.

Effect of Noble Metal Coating Type on the Photodegradation of MB

The SPR effect associated with the type of noble metal coating on the photocatalytic performance of these composite PC structures was studied by coating TiO_2-NAA-DBRs fabricated with T_P = 985 s and t_{pw} = 24 min with thin films of Au and Ag with varying deposition time (τ_D), from 0 to 60 s with $\Delta\tau_D$ = 30 s. Optical transmission of these composite PC structures was characterized and analyzed. **Table S2** (**ESI**) and **Fig. 8** summarize the effect of Au and Ag coatings on the kinetic constant and optical transmission of noble metal-coated TiO_2-functionalized NAA-DBRs. **Figs. 8a** and **b** show the transmission spectra of Au- and Ag-TiO_2-NAA-DBRs as a function of τ_D, respectively. In general, the intensity of the characteristic PSB of these noble metal-TiO_2-NAA-DBRs decreases with increasing τ_D due to the absorption by the nanoporous metallic layer deposited on the top surface of these composite PCs. These PC structures show 1st and 2nd order characteristic PSBs, which are denoted by the red and purple shaded regions in **Figs. 8a** and **b**, and also characteristic SPR bands for Au- and Ag-TiO_2-NAA-DBRs located at 497 ± 1 nm and 335 ± 1 nm, respectively. Magnified views of the characteristic PSBs (shaded regions in **Figs. 8a** and **b**) for Au- and Ag-TiO_2-NAA-DBRs are shown in **Figs. 8c** and **d**, respectively. **Fig. 8c** shows that the change in the position of the 1st and 2nd order PSBs of Au-TiO_2-NAA-DBRs with the Au coating is almost negligible, in consistency with our previous observations (**Fig. 7**). On the other hand, **Fig. 8d** shows that the features of the 1st and 2nd order PSBs of Ag-TiO_2-NAA-DBRs blue-shift their position and broaden their width with increasing τ_D. **Figs. 8e** and **f** summarize the photocatalytic performance of Au- and Ag-TiO_2-NAA-DBRs as a function of τ_D in terms of linearized pseudo-first order kinetics for the photodegradation of MB, where the insets correspond to the photocatalytic degradation rates (*k* – slopes of linear fittings) of each system. These results demonstrate that the photocatalytic degradation rate of MB by both Au- and Ag-TiO_2-NAA-DBRs worsens with increasing τ_D. The *k* values achieved by Au-TiO_2-NAA-DBRs produced at τ_D = 0, 30 and 60 s were 1.67 ± 0.05, 1.54 ± 0.07 and 1.41 ± 0.06 h^{-1}, respectively. These results demonstrate that non-coated TiO_2-NAA-DBRs outperform their Au-coated counterparts by a 7–16 % superior

performance in degrading MB. Ag-TiO_2-NAA-DBRs synthesized with τ_D = 0 s have the highest *k* value (i.e. 1.67 ± 0.05 h^{-1}) when compared to Ag-coated analogues fabricated with τ_D = 30 and 60 s, which achieve *k* values of 1.44 ± 0.06 and 1.35 ± 0.05 h^{-1}, respectively. It is thus clear that non-coated TiO_2-NAA-DBRs provide a 14–19 % superior performance in degrading MB than that of Ag-coated composite PCs. In summary, Au-TiO_2-NAA-DBRs perform more efficiently than Ag-TiO_2-NAA-DBRs at any τ_D. Ag nanostructures provide enhanced SPR effects as compared to their Au-based counterparts. However, the chemical stability of Au against surface oxidation and dissolution in aqueous environments makes Au-TiO_2-NAA-DBRs superior platforms to photodegrade MB molecules.

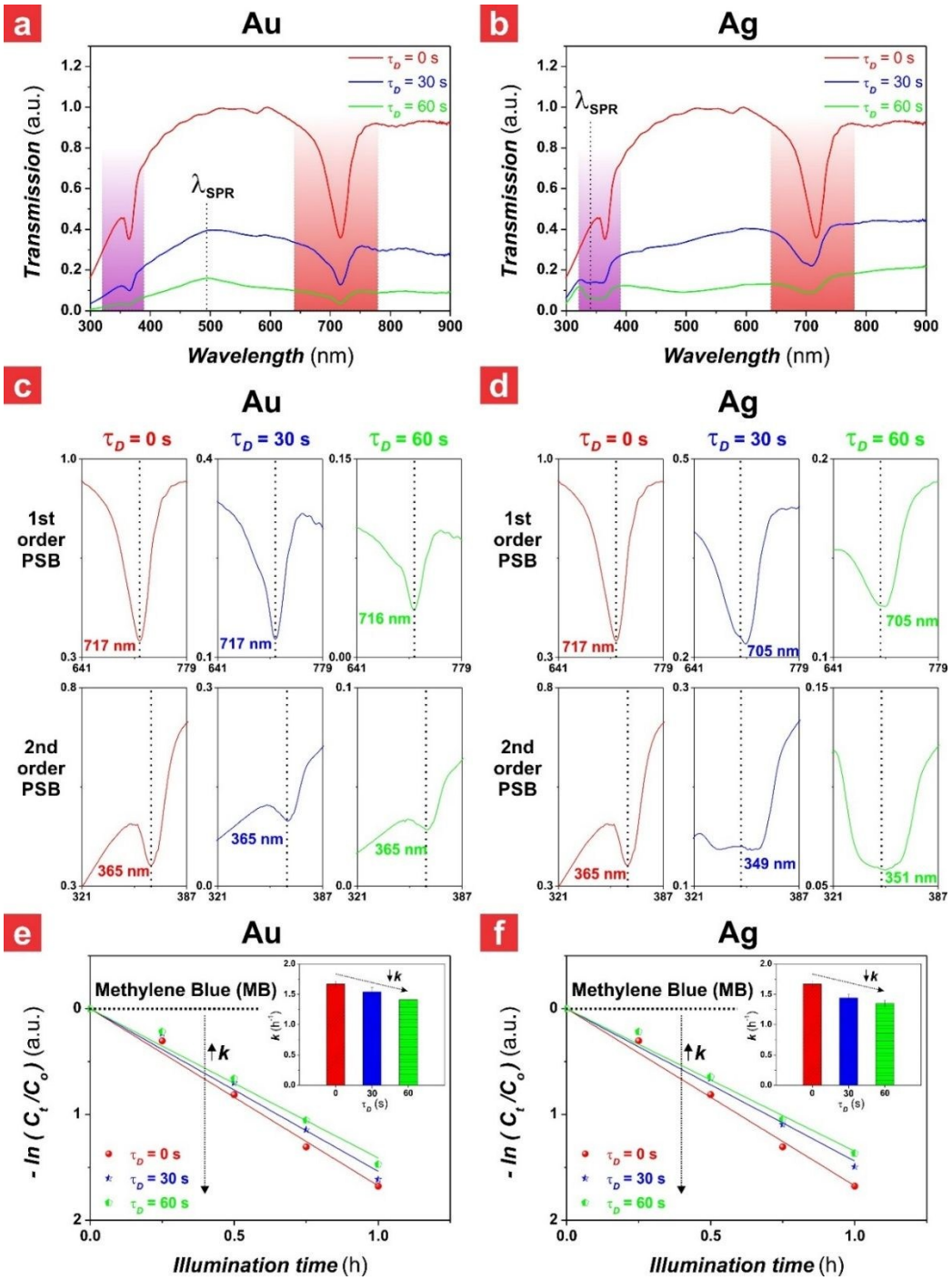

Fig. 8 Optical characterization and photocatalytic degradation assessment of Au- and Ag-TiO_2-NAA-DBRs produced with T_P = 985 s and t_{pw} = 24 min. a-b) Transmission spectra of Au- and Ag-TiO_2-NAA-DBRs as a function of the deposition time (τ_D), respectively (note: medium = air). c-d) Magnified views of the photonic stopbands (PSBs) of Au- and Ag-TiO_2-NAA-DBRs from the shaded regions shown in (a) and (b) at different τ_D, respectively. e-f) Photocatalytic degradation kinetics of methylene blue (MB) in Au- and Ag-TiO_2-NAA-DBRs, respectively (note: black dotted lines correspond to the photocatalytic degradation of MB in control NAA-DBRs without the photoactive TiO_2 layer with insets compiling the values of the kinetic constant (*k*) for MB).

View Article Online
DOI: 10.1039/C9CY00627C

Effect of Geometric Features of Au-TiO_2-NAA-DBRs on the Photocatalytic Degradation of MB

The position of the SPR band of Au-TiO_2-NAA-DBRs (λ_{SPR}) can be readily controlled by modifying the pore diameter (d_p) and interpore distance (d_{int}) of nanopores at the top plane of NAA-DBRs (horizontal plane – **Fig. 2a**). To demonstrate the tuneability and effect of the position of the SPR band on the photodegradation of MB, the geometric features (i.e. d_p and d_{int}) of Au-TiO_2-NAA-DBRs at the top horizontal plane were systematically modified by a three-step anodization approach, in which the starting anodization voltage (V_o) and Au deposition time (τ_D) were modified from V_o = 60 to 100 V with ΔV_o = 20 V, and from τ_D = 0 to 60 s with $\Delta\tau_D$ = 30 s. Fabrication parameters of the third anodization step (i.e. pulse anodization mode) were fixed to T_P = 985 s, number of pulses = 60 pulses, and t_{pw} = 0 min to maintain the position and features of the characteristic PSB, which are established by the period length (L_{TP}) along the normal plane of the NAA-DBR structure. **Fig. S11** (**ESI**) demonstrates that the PSB of these PCs in the reflection spectrum does not change its position significantly with varying V_o, both in air and water. The average λ_C in Au-TiO_2-NAA-DBRs in air and water were 835 ± 14 and 865 ± 9 nm, respectively. Under such configuration, the characteristic PSB is located outside of the absorbance band of MB and therefore the photocatalytic system is independent on the "slow photon" effect. **Table S3** (**ESI**) and **Fig. 9** summarize the correlation of the photocatalytic performance of Au-TiO_2-NAA-DBRs with V_o and τ_D.

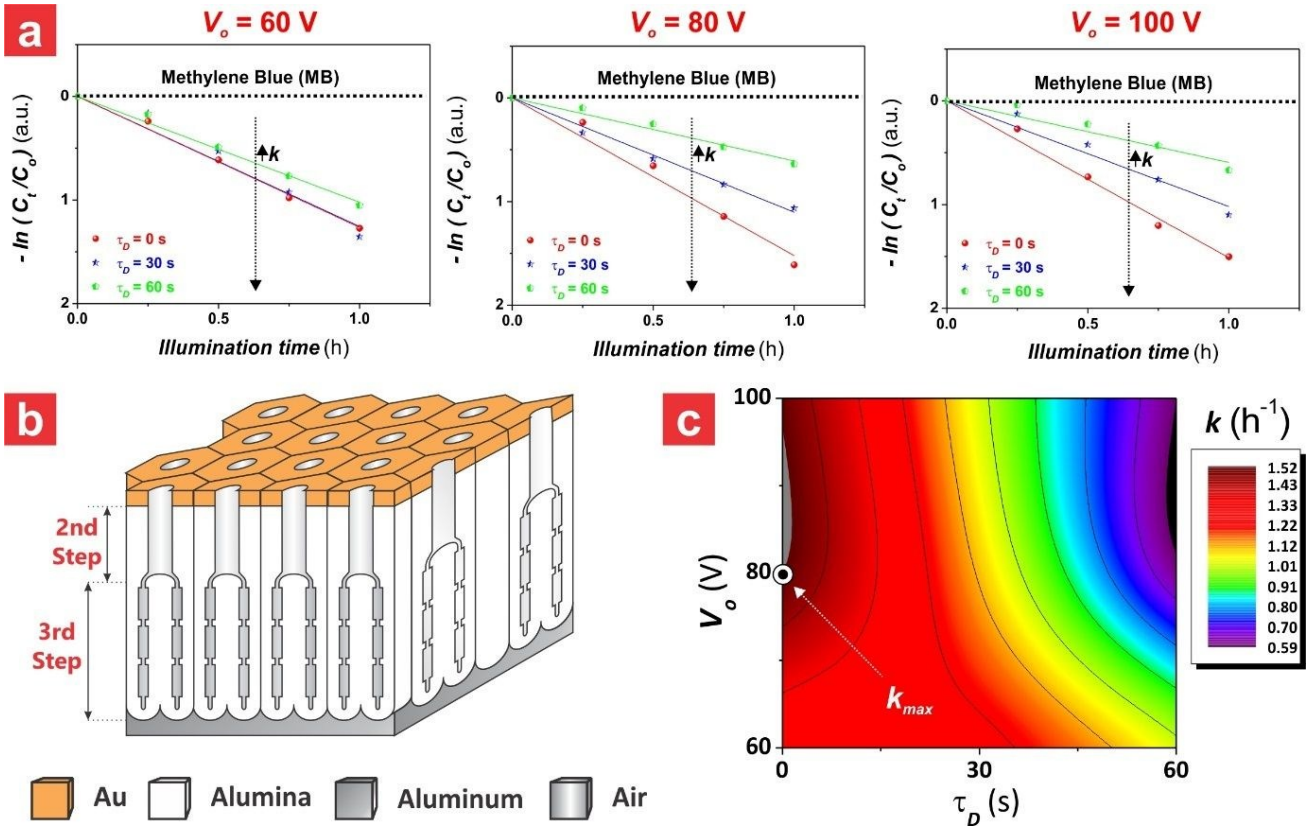

Fig. 9 Combinational effect of starting anodization voltage (V_o) and Au deposition time (τ_D) on the kinetic constant (k) for the photodegradation of methylene blue (MB) by Au-TiO_2-NAA-DBRs. a) Photocatalytic degradation kinetics of MB by Au-TiO_2-NAA-DBRs fabricated by three-step pulse anodization with τ_D = 0, 30 and 60 s and anodization voltage (V_o) of 60 V (left), 80 V (center) and 100 V (right) (note: black dotted lines correspond to the photodegradation of MB in control NAA-DBRs without the photoactive TiO_2 layer). b) Schematic of the nanoporous structures of NAA-DBRs fabricated by three-step pulse anodization. c) Contour map showing the combined effect of V_o and τ_D on k values for the photodegradation of MB by Au-TiO_2-NAA-DBRs.

Fig 9a presents the photocatalytic degradation kinetics of MB as a function of V_o and τ_D, in which the slope of the fitting lines corresponds to k – indicator of photocatalytic performance. As these results demonstrate, in general k decreases with increasing τ_D. This can be attributable to the isolated position of the nanoporous Au layer on the top plane of the composite PC structures. The Au thin film acts as a screen that absorbs the majority of the incoming light and prevents its efficient propagation across the bulk Au-TiO_2-NAA-DBR structure, minimizing the overall photocatalytic performance due to a localized generation of SPR-excited photons on the top surface (i.e. photons are not transferred efficiently to the photoactive TiO_2 layer). **Fig. 9b** illustrates the idealized structure of Au-TiO_2-NAA-DBRs fabricated by three-step pulse anodization, in which the high starting anodization voltage in the second step is followed by a reduction of

anodization voltage during the third step that leads to branching of nanopores. The contour graph shown in **Fig. 9c** summarizes the dependency of the photocatalytic performance of Au-TiO_2-NAA-DBRs on V_o and τ_D. The smooth and homogeneous distribution of color fields and field lines implies a relatively weak dependence of k on these fabrication parameters, though the effect of V_o on k is less significant than that of τ_D. The maximum and minimum of k (1.52 ± 0.07 and 0.59 ± 0.06 h^{-1}) are located at V_o = 80 V and τ_D = 0 s, and V_o = 100 V and τ_D = 60 s, respectively. The k_{max} (1.51 ± 0.05 h^{-1}) located at V_o = 100 V and τ_D = 0 s is statistically the same than the maximum of k observed at V_o = 80 V and τ_D = 0 s, with only ~1% of difference. In contrast, the k (1.26 ± 0.03 h^{-1}) located at V_o = 60 V is ~17 % smaller than that achieved by Au-TiO_2-NAA-DBRs produced at V_o = 80 and 100 V. It is also worth noting that the photocatalytic performance of Au-TiO_2-NAA-DBRs produced with V_o = 60 V is relatively similar with increasing τ_D as compared to the significant decrease observed in Au-TiO_2-NAA-DBRs produced with V_o = 80 and 100 V. The average k value of Au-TiO_2-NAA-DBRs produced with V_o = 60 V at various τ_D was found to be 1.18 ± 0.14 h^{-1}.

Table 1 summarizes the geometric characteristics – d_p and d_{int} – of Au-TiO_2-NAA-DBRs produced at different V_o, and the percentage decrement in k as a function of the fabrication parameters – V_o and τ_D –. The d_p and d_{int} of nanopores at the top surface of Au-TiO_2-NAA-DBRs (τ_D = 0 s) increase with increasing V_o (i.e. from 70 to 150 nm and from 157 to 272 nm, respectively). Larger d_p and d_{int} enhance the absorption of light by the PC structure, increasing the photogeneration of e^-/h^+ pairs in the photoactive TiO_2 layer and improving the photocatalytic performance of Au-TiO_2-NAA-DBRs (τ_D = 0 s). This effect is demonstrated by the k values observed for Au-TiO_2-NAA-DBRs produced with V_o = 60, 80 and 100 V (**Fig. 9c**). k decreases slightly with increasing τ_D for Au-TiO_2-NAA-DBRs produced with V_o = 60 V, with an average reduction of photocatalytic performance of ~1% and 19% when τ_D is varied from 0 to 30 s and from 0 to 60 s, respectively. However, Au-TiO_2-NAA-DBRs fabricated with V_o = 80 and 100 V show a significantly higher reduction in k with τ_D (i.e. ~28% and 60% for τ_D from 0 to 30 s, and ~33% and 61% for τ_D from 0 to 60 s, respectively).

Table 1. Effect of the starting anodization voltage (V_o) of Au-TiO_2-NAA-DBRs produced by three-step pulse anodization on the pore diameter (d_p), interpore distance (d_{int}) and the decrease in percentage of kinetic constant (k) at different Au deposition times (τ_D), from 0 to 60 s.

V_o (V)	d_p (nm)	d_{int} (nm)	k decrement from τ_D = 0 to 30 s (%)	k decrement from τ_D = 0 to 60 s (%)
60	70 ± 1	157 ± 1	1	19
80	106 ± 1	211 ± 2	28	60
100	150 ± 1	272 ± 3	33	61

Photocatalytic Degradation Mechanism

Based on these results, we propose a possible photocatalytic degradation mechanism to describe the photocatalytic degradation of organic dye by Au-TiO_2-NAA-DBRs driven under visible–NIR irradiation (400–1025 nm) with the addition of H_2O_2. Upon light irradiation, charge carriers (i.e. electrons and holes) are produced in the conduction and valence bands, respectively, of the photoactive TiO_2 layer deposited onto the inner surface of Au-TiO_2-NAA-DBRs. Photogenerated holes induce oxidation of H_2O in the aqueous organic solution, which is in contact with the photoactive TiO_2 layer. This generates $OH^{\cdot}$ radicals, which can degrade the organic dye molecules to liberate CO_2 and H_2O. Photogenerated electrons also react with H_2O_2 to produce $OH^{\cdot}$ radicals and OH^- ions, of which the latter are oxidized into $OH^{\cdot}$ radicals by photogenerated holes in the valence band of the photoactive TiO_2 layer. Our results indicate that enhancements in the photodegradation of methylene blue are strongly associated with slow photons in Au-TiO_2-NAA-DBRs. This light–matter interaction increases the lifespan of incoming photons with specific energies (i.e. wavelengths close to the blue and red edges of the PSB), which spend longer time within the structure of Au-TiO_2-NAA-DBRs. This can then be exploited more efficiently by the photoactive TiO_2 layer to generate extra e^-/h^+ pairs that speed up the photocatalytic degradation of MB. The photocatalytic enhancement associated with this effect is found to be maximum when the edges of the characteristic PSB of Au-TiO_2-NAA-DBRs are in close proximity to the blue and red sides of the absorbance band of MB. Overlapping the PSB with the absorbance maximum of MB worsens dramatically the performance of Au-TiO_2-NAA-DBRs due to light screening effect, since in this spectral region only a small portion of the incoming light reaches the photoactive TiO_2 layer to generate extra e^-/h^+ pairs that can be utilized by the composite PC structures to photodegrade MB molecules. Deposition of a thin Au layer on the top surface of TiO_2-NAA-DBRs provides an additional feature to the system in the form of a surface plasmon resonance band, which extends the overall light absorption of the non-coated TiO_2-NAA-DBR structure. However, SPR-excited photons generated by the Au layer deposited on the top surface of Au-TiO_2-NAA-DBRs are not fully utilized by the photocatalytic platform due to the isolated configuration between the Au layer and the photoactive TiO_2 layer in the inner surface of the composite PC structure. The majority of the incoming light is absorbed by the nanoporous Au layer before it reaches the photoactive surface of TiO_2-NAA-DBRs, and the overall photocatalytic performance of Au-TiO_2-NAA-DBRs decreases with the thickness of the Au layer (i.e. more light is absorbed by the Au layer). Our analysis also demonstrates that, though Ag has a better SPR than Au, Au-TiO_2-NAA-DBRs perform better than their Ag-coated counterparts. This is due to the higher chemical stability of Au in aqueous solution. The overall photocatalytic performance of Au-TiO_2-NAA-DBRs can be enhanced by engineering the geometric features (i.e. d_p, d_{int}, L_{TP} and L_p) of these nanoporous composite semiconductor PC structures. The rational design of Au-TiO_2-NAA-DBRs enables an efficient management of photons by "slow photon" and SPR effects, tuning the relative position of the edges of the characteristic PSB and SPR with respect to the absorbance band of MB.

View Article Online
DOI: 10.1039/C9CY00627C

Comparison with Benchmark Photocatalyst Materials

Table 2 compiles the photocatalytic performances of representative benchmark photocatalytic materials with and without noble metal (i.e. Ag) and photonic crystal structure (i.e. inverse opal and DBR), where the photodegradation of MB molecules were conducted under visible light irradiation conditions.

Table 2. Compilation of representative kinetic constants (*k*) for the photocatalytic degradation of MB molecules by various benchmark TiO_2-based photocatalyst materials.

TiO_2-based Photocatalyst	*k* (h^{-1})	Ref
P25 Nanoparticles	0.64	4
Inverse Opal	1.32	4
NAA-DBRs	2.45	This Study
Ag-P25 Nanoparticles	1.56	6
Ag-Inverse Opal	0.64	8
Ag-NAA-DBRs	1.44	This Study

The photocatalytic degradation rate of MB by as-produced P25 TiO_2 nanoparticles, TiO_2 inverse opals and TiO_2-NAA-DBRs were found to be 0.64, 1.32 and 2.45 h^{-1}, respectively.[4] It is clear that TiO_2-NAA-DBR performs more efficiently than these reference materials, with a ~74 and 46% superior performance, respectively. Incorporation of SPR effects in noble metal-coated photocatalysts can enhance their performance due to extended light absorption and minimization of charge carrier recombination rates. The *k* values for Ag-coated P25 TiO_2 nanoparticles, TiO_2 inverse opals and TiO_2-NAA-DBRs were found to be 1.56, 0.64 and 1.44 h^{-1}, respectively.[6,8] This demonstrates that Ag-P25 TiO_2 nanoparticles perform much better than Ag-TiO_2 inverse opals (~59% superior performance), and slightly better than Ag-TiO_2-NAA-DBRs (~8% superior performance) in the photodegradation of MB. This result can be associated with a better interfacial connection between the noble metal coating and the semiconductor material in Ag-P25 TiO_2. However, Ag-TiO_2-NAA-DBRs outperform Ag-TiO_2 inverse opals by ~56% enhancement. A direct comparison with these studies could not be completely correct due to small differences in experimental conditions (i.e. loading of catalysts, spectral distribution and power of light illumination, specific area and volume). However, these results demonstrate that TiO_2-NAA-DBRs are promising photocatalyst platforms that provide new opportunities to develop high-performing photocatalyst materials with broad applicability.

Conclusions

This study provides new insights into the design and engineering of high-performing photocatalyst platforms with rationally designed optical properties to harness light–matter interactions for photocatalysis. The photocatalytic capabilities of NAA-based photonic crystals functionalized with photoactive layers of TiO_2 and noble metal coatings have been systematically assessed, using the degradation rate of a model organic dye as an indicator to identify enhancements associated with different optical phenomena. Noble metal-TiO_2-NAA-DBRs were produced with various fabrication parameters (i.e. anodization period, starting anodization voltage, pore widening time, noble metal deposition time and type of noble metal coating) to enable the fine-tuning of the optical properties (i.e. position and features of PSB and SPR bands) of these composite PC structures across the spectral regions. Our results indicate that the best photocatalytic degradation rate for methylene blue (i.e. k = 2.45 h^{-1}) is achieved by Au-TiO_2-NAA-DBRs produced with V_o = 40 V, T_P = 895 s, t_{pw} = 24 min and τ_D = 0 s. Enhancements in photocatalytic performance are strongly dependent on the "slow photon" effect, being optimal when the edges of the characteristic PSB of Au-TiO_2-NAA-DBRs are partially overlapped with the absorbance band of methylene blue, but away from its maximum to avoid undesired light screening effect. Photodegradation rate enhancements in noble metal-TiO_2-NAA-DBRs are independent of "slow photon" effect when the characteristic PSB is completely outside of the absorbance band of MB. Under such a configuration, enhancements are solely dependent on the total pore length of the noble metal-TiO_2-NAA-DBR, and the thicker the PC structure the more efficient the photocatalytic performance. This study also reveals that enhancements in the photocatalytic performance of noble metal-TiO_2-NAA-DBRs by SPR in the noble metal layer are not significant due to the isolated behavior of the nanoplasmonic structure, which is localized in the top surface of the composite PC structures. As a result, the majority of light is absorbed in the metallic coating before it reaches the bulk PC structure, worsening the overall photocatalytic performance. The type of noble metal coating (i.e. Ag and Au) also plays a critical role in the overall photocatalytic performance of noble metal-TiO_2-NAA-DBRs, where Au coatings are demonstrated to provide superior performance than that of Ag coatings due to the higher chemical stability of Au in aqueous solution. This study also demonstrates that the photocatalytic performance of non-coated TiO_2-NAA-DBRs enhances with increasing pore diameter and interpore distance through enhanced light scattering and absorption.

In summary, a rational and optimal design of noble metal-TiO_2-NAA-DBRs is essential to efficiently utilize and manage "slow photon" and SPR effects for photocatalytic reactions. This study provides a strong foundation for improving the design of NAA-based photoactive photonic crystals, generating new opportunities to spread the applicability of these engineered materials across various photocatalytic applications such as sanitation of water, production of clean hydrogen and carbon dioxide reduction.

Acknowledgements

Authors thank the support provided by the Australian Research Council (ARC) through the grant number CE140100003, the School of Chemical Engineering, the University of Adelaide (UoA), the Institute for Photonics and

Advanced Sensing (IPAS), and the ARC Centre of Excellence for Nanoscale BioPhotonics (CNBP). Authors thank the Adelaide Microscopy (AM) centre for FEG-SEM and EDX characterization.

1 K. Kim, P. Thiyagarajan, H.-J. Ahn, S.-I. Kim, J.-H. Jang, *Nanoscale*, 2013, **5**, 6254-6260.
2 R. Bopella, S.T. Kochuveedu, H. Kim, M.J. Jeong, F. Marques Mota, J. H. Park, D. H. Kim, *ACS Appl. Mater. Interfaces*, 2017, **9**, 7075-7083.
3 M. Zhou, J. Bao, Y. Xu, J. Zhang, J. Xie, M. Guan, C. Wang, L. Wen, Y. Lei, Y. Xie, *ACS Nano*, 2014, **8**, 7088-7098.
4 X. Zheng, S. Meng, J. Chen, J. Wang, J. Xian, Y. Shao, X. Fu, D. Li, *J. Phys. Chem. C*, 2013, **117**, 21263-21273.
5 Y. Lu, H. Yu, S. Chen, X. Quan, H. Zhao, *Environ. Sci. Technol.*, 2012, **46**, 1724-1730.
6 S. Ko, C. K. Banerjee, J. Sankar, *Compos. Part B – Eng*, 2011, **42**, 579-583.
7 Z. Cai, Z. Xiong, X. Lu, J. Teng, *J. Mater. Chem. A*, 2014, **2**, 545-553.
8 Z. Chen, L. Fang, W. Dong, F. Zheng, M. Shen, J. Wang, *J. Mater. Chem. A*, 2014, **2**, 824-832.
9 S. Meng, D. Li, L. Fu, X. Fu, *J. Mater. Chem. A*, 2015, **3**, 23501-23511.
10 S. Y. Lim, C. S. Law, M. Markovic, L. F. Marsal, N. H. Voelcker, A. D. Abell, A. Santos, *ACS Appl. Energy Mater.*, 2019, **2**, 1169-1184.
11 S. Y. Lim, C. S. Law, M. Markovic, J. K. Kirby, A. D. Abell, A. Santos, *ACS Appl. Mater. Interfaces*, 2018, **10**, 24124-24136.
12 M. Curti, C. B. Mendive, M. A. Grela, D. W. Bahnemann, *Mater. Res. Bull.*, 2017, **9**, 155-165.
13 S. Zhao, Z. Qu, N. Yan, Z. Li, W. Zhu, J. Pan, J. Xu, M. Li, *RSC Adv.*, 2015, **5**, 30841-30850.
14 H. Hirakawa, M. Hashimoto, Y. Shiraishi, T. Hirai, *J. Am. Chem. Soc.*, 2017, **139**, 10929-10936.
15 J. Yang, Y. Guo, R. Jiang, F. Qin, H. Zhang, W. Lu, J. Wang, J. C. Yu, *J. Am. Chem. Soc.*, 2018, **140**, 8497-8508.
16 W. Hou, W. H. Hung, P. Pavaskar, A. Goeppert, M. Aykol, S.B. Cronin, *ACS Catal.*, 2011, **1**, 929-936.
17 J. Jiao, Y. Wei, K. Chi, Z. Zhao, A. Duan, J. Liu, G. Jiang, Y. Wang, X. Wang, C. Han, P. Zheng, *Energy Technol.*, 2017, **5**, 877-883.
18 V. Štengl, T. M. Grygar, F. Opluštil, T. Němec, *J. Hazard Mater.*, 2012, **227-228**, 62-67.
19 A. Sengele, D. Robert, N. Keller, V. Keller, A. Herissan, C. Colbeau-Justin, *J. Catal.*, 2016, **334**, 129-141.
20 A. Fujishima, K. Honda, *Nature*, 1972, **238**, 37-38.
21 J. H. Carey, J. Lawrence, H. M. Tosine, *Bull. Environ. Contam. Toxicol.*, 1976, **16**, 697-701.
22 M. Anpo, *Catal. Surv. Jpn.*, 1997, **1**, 169-179.
23 X. Chen, S. S. Mao, *Chem. Rev.*, 2007, **107**, 2891-2959.
24 R. Asahi, T. Morikawa, T. Ohwaki, K. Aoki, Y. Taga, *Science*, 2001, **293**, 269-271.
25 W. Choi, A. Termin, M. R. Hoffmann, *J. Phys. Chem.*, 1994, **98**, 13669-13679.
26 Y. Liu, L. Yu, Y. Hu, C. Guo, F. Zhang, X. W. Lou, *Nanoscale*, 2012, **4**, 183-187.
27 M. Zalfani, B. van der Schueren, Z.-Y. Hu, J. C. Rooke, R. Bourguiga, M. Wu, Y. Li, G. V. Tendeloo, B.-L. Su, *J. Mater. Chem. A*, 2015, **3**, 21244-21256.
28 H. Fu, T. Xu, S. Zhu, Y. Zhu, *Environ. Sci. Technol.*, 2008, **42**, 8064-8069.
29 D. Jian, P.-X. Gao, W. Cai, B. S. Allimi, S. P. Alpay, Y. Ding, Z. L. Wang, C. Brooks, *J. Mater. Chem.*, 2009, **19**, 970-975.
30 J. G. Yu, Y. R. Su, B. Cheng, *Adv. Funct. Mater.*, 2007, **17**, 1984-1990.
31 R. Bleta, P. Alphonse, L. Lorenzato, *J. Phys. Chem. C*, 2010, **114**, 2039-2048.
32 T. Hirakawa, P. V. Kamat, *J. Am. Chem. Soc.*, 2005, **127**, 3928-3934.
33 X. Zhou, G. Liu, J. Yu, W. Fan, *J. Mater. Chem.*, 2012, **22**, 21337-21354.
34 S. K. Ghosh, T. Pal, *Chem. Rev.*, 2007, **107**, 4797-4862.
35 J. E. G. J. Wijnhoven, W. L. Vos, *Science*, 1998, **281**, 802-804.
36 Z. Zhang, L. Zhang, M. N. Hedhili, H. Zhang, P. Wang, *Nano Lett.*, 2013, **13**, 14-20.
37 C.-T. Dinh, H. Yen, F. Kleitz, T.-O. Do, *Angew. Chem. Int. Ed.*, 2014, **53**, 6618-6623.
38 Y. Wang, D.-B. Xiong, W. Zhang, H. Su, Q. Liu, J. Gu, S. Zhu, D. Zhang, *Catalysis Today*, 2016, **274**, 15-21.
39 E. Yablonovitch, *Phys. Rev. Lett.*, 1987, **58**, 2059.
40 J. Liu, H. Zhao, M. Wu, B. Van der Schueren, Y. Li, O. Deparis, J. Ye, G. A. Ozin, T. Hasan, B.-L. Su, *Adv. Mater.*, 2017, **29**, 1605349.
41 M. Curti, J. Schneider, D. W. Bahnemann, C. B. Mendive, *J. Phys. Chem. Lett.*, 2015, **6**, 3903-3910.
42 A. Steins, B. E. Wilson, S. G. Rudisill, *Chem. Soc. Rev.*, 2013, **42**, 2763-2803.
43 D. P. Gaillot, C. J. Summers, in *Atomic Layer Deposition of Nanostructured Materials*, ed. N. Pinna, M. Knez, Wiley-VCH, Weinheim, 1st edn, 2012, ch. 15, pp. 345-371.
44 V. Likodimos, *Appl. Catal. B*, 2018, **230**, 269-303.
45 K. Lee, A. Mazare, P. Schmuki, *Chem. Rev.*, 2014, **114**, 9385-9454.
46 J. W. Galusha, C.-K. Tsung, G. D. Stucky, M. H. Bartl, *Chem. Mater.*, 2008, **20**, 4925-4930.
47 C.S. Law, S. Y. Lim, A. Santos, *Sci. Rep.*, 2018, **8**, 4642.
48 A. Santos, T. Peirera, C. S. Law, D. Losic, *Nanoscale*, 2016, **8**, 14846-14857.
49 Sukarno, C. S. Law, A. Santos, *Nanoscale*, 2017, **9**, 7541-7550.
50 C. S. Law, G. M. Sylvia, M. Nemati, J. Yu, D. Losic, A. D. Abell, A. Santos, *ACS Appl. Mater. Interfaces*, 2017, **9**, 8929-8940.
51 C. S. Law, S. Y. Lim, A. D. Abell, A. Santos, *Anal. Chem.*, 2018, **90**, 10039-10048.
52 A. Santos, J. H. Yoo, C. V. Rohatgi, T. Kumeria, Y. Wang, D. Losic, *Nanoscale*, 2016, **8**, 1360-1373.
53 A. Santos, C. S. Law, D. W. C. Lei, T. Pereira, D. Losic, *Nanoscale*, 2016, **8**, 18360-18375.
54 A. Santos, C. S. Law, T. Pereira, D. Losic, Nanoscale, 2016, **8**, 8091-8100.
55 S. Y. Lim, C. S. Law, L. F. Marsal, A. Santos, *Sci. Rep.*, 2018, **8**, 9455.
56 Y. Wang, Y. Chen, T. Kumeria, F. Ding, A. Evdokiou, D. Losic, A. Santos, *ACS Appl. Mater. Interfaces*, 2015, **7**, 9879-9888.
57 C. S. Law, S. Y. Lim, A. D. Abell, L. F. Marsal, A. Santos, *Nanoscale*, 2018, **10**, 14139-14152.
58 C. S. Law, S. Y. Lim, R. M. Macalincag, A. D. Abell, A. Santos, *ACS Appl. Nano Mater.*, 2018, **1**, 4418-4434.
59 M. M. Rahman, L. F. Marsal, J. Pallarès, J. Ferré-Borrull, *ACS Appl. Mater. Interfaces*, 2013, **5**, 13375-13381.
60 M. D. Abràmoff, P. J. Magalhães, S. J. Ram, *Biophotonics Inter.*, 2004, **11**, 36-42.
61 A. Santos, *J. Mater. Chem. C*, 2017, **5**, 5581-5599.
62 S. Nishimura, N. Abrams, B. A. Lewis, L. I. Halaoui, T. E. Malluok, K. D. Benkstein, J. van de Lagemaat, A. J. Frank, *J. Am. Chem. Soc.*, 2003, **125**, 6306-6310.
63 Y. Li, T. Kunitake, S. Fujikawa, *J. Phys. Chem. B*, 2006, **110**, 13000-13004.
64 O. Deparis, S. R. Mouchet, B.-L. Su, *Phys. Chem. Chem. Phys.*, 2015, **17**, 30525-30532.
65 H. Zhao, Z. Hui, J. Liu, Y. Li, M. Wu, G. V. Tendeloo, B.-L. Su, *Nano Energy*, 2018, **47**, 266-274.
66 A. Santos, V. S. Balderrama, M. Alba, P. Formentín, J. Ferré-

Borrull, J. Pallarès, L. F. Marsal, *Adv. Mater.*, 2012, **24**, 1050-1054.

67 A. Brzózka, A. Brudzisz, K. Hnida, G. D. Sulka, in *Electrochemically Engineered Nanoporous Materials: Methods, Properties and Applications*, ed. D. Losic, A. Santos, Springer International Publishing, Cham, 2015, vol. 220, ch. 8, pp. 219-288.

View Article Online
DOI: 10.1039/C9CY00627C